The Use of Exergy and Decomposition Techniques in the Development of Generic Analysis and Optimization Methodologies Applicable to the Synthesis/Design of Aircraft / Aerospace Systems

Prof. Michael R. von Spakovsky

Graduate Students: **Vijayanand Periannan, Kyle C. Markell, Keith M. Brewer**

Center for Energy Systems Research

Mechanical engineering Department

Virginia Tech

Blacksburg, Virginia 24061

Contract No. F 49620-03-1-0189

AFOSR/NA Directorate

Program manager: John Schmisseur

REPORT DOCUMENTATION PAGE

Form Approved
OMB No. 0704-0188

1. REPORT DATE *(DD-MM-YYYY)*	2. REPORT TYPE	3. DATES COVERED *(From - To)*
21-04-2006	Final Report – 3 M.S. Theses	April 1, 2003 to April 21, 2006

4. TITLE AND SUBTITLE **Project Title**: The Use of Exergy and Decomposition Techniques in the Development of Generic Analysis and Optimization Methodologies Applicable to the Synthesis/Design of Aircraft / Aerospace Systems; **Thesis #1**: Investigation of the Effects of Different Objective Functions/Figures of Merit on the Analysis and Optimization of High Performance Aircraft System Synthesis/Design; **Thesis #2**: Exergy Methods for the Generic Analysis and Optimization of Hypersonic Vehicle Concepts; **Thesis #3**: Exergy Methods for the Mission-Level Analysis and Optimization of Generic Hypersonic Vehicles

5a. CONTRACT NUMBER
F 49620-03-1-0189

5b. GRANT NUMBER

5c. PROGRAM ELEMENT NUMBER

6. AUTHOR(S)
von Spakovsky, Michael R. (professor and theses advisor)
Periannan, Vijayanand (graduate student)
Markell, Kyle C. (graduate student)
Brewer, Keith M. (graduate student)

5d. PROJECT NUMBER

5e. TASK NUMBER

5f. WORK UNIT NUMBER

7. PERFORMING ORGANIZATION NAME(S) AND ADDRESS(ES)
Center for Energy Systems Research
M.E. Dept. (0238)
Virginia Tech
Blacksburg, VA 24060

8. PERFORMING ORGANIZATION REPORT NUMBER
208-11-110F-107-353-1
FRS # 430029

9. SPONSORING / MONITORING AGENCY NAME(S) AND ADDRESS(ES)
Air Force Office of Sponsored Programs
AFOSR/ NA Directorate
801 N. Randolph St., Room 732
Arlington, VA 22203-1977
Tel.: (703) 696-6962 Dr John Schmisseur

10. SPONSOR/MONITOR'S ACRONYM(S)
AFOSR/NA

11. SPONSOR/MONITOR'S REPORT NUMBER(S)

12. DISTRIBUTION / AVAILABILITY STATEMENT

AFRL-SR-AR-TR-06-0492

Approved for public release;
distribution unlimited

13. SUPPLEMENTARY NOTES
None

14. ABSTRACT

In M.S. thesis #1, the advantages of applying exergy-based analysis and optimization methods to the synthesis/design and operation of aircraft systems is demonstrated using a supersonic aircraft fighter flown over an entire mission. A first set of optimizations involving four objectives (two energy-based and two exergy-based) are performed with only propulsion and environmental control subsystem degrees of freedom. Losses for the airframe subsystem are not incorporated into the two exergy-based objectives. The results show that as expected all four objectives globally produce the same optimum vehicle. A second set of optimizations is then performed with airframe degrees of freedom. However, this time one of the exergy-based objectives incorporates airframe losses directly into the objective. The results are that this latter objective produces a significantly better optimum vehicle. Thus, an exergy-based approach is not only able to pinpoint where the greatest inefficiencies in the system occur but seems to produce a superior optimum vehicle as well by accounting for irreversibility losses in subsystems only indirectly tied to fuel usage.

Though the field of hypersonic vehicle design is thriving again, no studies to date of which we are aware demonstrate the technology through an entire mission in which multiple flight conditions and constraints are encountered. This is likely due to the highly integrated and sensitive nature of hypersonic vehicle components. Consequently, in M.S. theses #2 and #3, a formal Mach 6 through Mach 10 flight envelope is explored which includes cruise, acceleration/climb, deceleration/descend and turn mission segments. An exergy approach to the vehicle synthesis/design, in which trade-offs between dissimilar technologies are observed, is proposed and measured against traditional energy-based methods of assessing highly integrated systems. The mission-level analysis provides much insight into the dynamics of mission-level hypersonic flight and demonstrates the usefulness of an exergy destruction minimization measure for highly integrated synthesis/design.

15. SUBJECT TERMS
exergy analysis, hypersonic vehicles, supersonic vehicles, synthesis/design, integrated mission level analysis and optimization, large-scale optimization, scramjets

16. SECURITY CLASSIFICATION OF:			17. LIMITATION OF ABSTRACT	18. NUMBER OF PAGES	19a. NAME OF RESPONSIBLE PERSON
a. REPORT	b. ABSTRACT	c. THIS PAGE			M. R. von Spakovsky
U	U	U	UU	474	19b. TELEPHONE NUMBER *(include area code)* 540 231-6684 / 6661

Standard Form 298 (Rev. 8-98)
Prescribed by ANSI Std. Z39.18

Abstract

The work summarized in this report and funded by this project reflects the work under my supervision of three M.Sc. level graduate students. A detailed description of each of these student's research is contained in three M.Sc. theses which can be downloaded from http://scholar.lib.vt.edu/theses/. The M.Sc. thesis titles and students' names are as follow: i) *Investigation of the Effects of Different Objective Functions/Figures of Merit on the Analysis and Optimization of High Performance Aircraft System Synthesis/Design* by Vijayanand Periannan; ii) *Exergy Methods for the Generic Analysis and Optimization of Hypersonic Vehicle Concepts* by Kyle Charles Markell; and iii) *Exergy Methods for the Mission-Level Analysis and Optimization of Generic Hypersonic Vehicles* by Keith Merritt Brewer.

In the first of these M.Sc. theses, the advantages of applying exergy-based analysis and optimization methods to the synthesis/design and operation of aircraft systems is demonstrated using an Advanced Aircraft Fighter (AAF) with three subsystems: a Propulsion Subsystem (PS), an Environmental Control Subsystem (ECS), and an Airframe Subsystem - Aerodynamics (AFS-A). Thermodynamic (both energy and exergy based), aerodynamic, geometric, and physical models of the components comprising the subsystems are developed and their interactions defined. Off-design performance is considered as well and is used in the analysis and optimization of system synthesis/design and operation as the aircraft is flown over an entire mission. An exergy-based parametric study of the PS and its components is first presented in order to show the type of detailed information on internal system losses which an exergy analysis can provide and an energy analysis by its very nature is unable to provide. This is followed by a series of constrained, system synthesis/design optimizations based on five different objective functions, which define energy-based and exergy-based measures of performance. The results show that an exergy-based approach is not only able to pinpoint where the greatest inefficiencies in the system occur but appears at least in this case to produce a superior optimum vehicle as well by accounting for irreversibility losses in subsystems (e.g., the AFS-A) only indirectly tied to fuel usage.

In the next two theses, both a partial scram-jet mission with three segments and a more complete scram-jet mission envelope of six segments ranging from Mach 6 through Mach 10 and including cruise, acceleration/climb, deceleration/descend, and turn mission segments are used in

the application of exergy-based analysis and optimization methods to integrated hypersonic vehicle synthesis/design. One-dimensional thermodynamic, geometric, aerodynamic, and physical models of the hypersonic vehicle and its two subsystems, i.e. the propulsion and airframe subsystems (PS and AFS-A), are developed and implemented. Mechanisms for loss are computed from such irreversible processes as shocks, friction, heat transfer, mixing, and incomplete combustion. The PS consists of inlet, combustor, and nozzle, while the AFS-A provides trim and force accounting measures. An energy addition mechanism, based on the potential of MHD technology, is utilized to maintain a shock-on-lip inlet operating condition throughout the missions (partial and complete). Thirteen decision variables (seven design and six operational) govern vehicle geometry and performance. Among the results are that optimizing the vehicle for the single most constrained mission segment in some cases yields a vehicle capable of flying the entire mission (in some cases not) but with fuel consumption and exergy destruction plus fuel loss values greater than those for the integrated vehicle solutions developed and presented here. In essence, mission-level analysis and optimization provides much insight into the dynamics of mission-level hypersonic flight and demonstrates the usefulness of an exergy destruction minimization measure for the highly integrated synthesis/design process.

Table of Contents

	Page
1. INVESTIGATION OF THE EFFECTS OF DIFFERENT OBJECTIVE FUNCTIONS/FIGURES OF MERIT	1
1.1 INTRODUCTION	1
1.2 PROPULSION SUBSYSTEM (PS) MODELS	2
1.3 ENVIRONMENTAL CONTROL SUB-SYSTEM (ECS) MODELS	3
1.4 AIRFRAME-AERODYNAMICS SUBSYSTEM (AFS-A) MODELS	4
1.5 SYSTEM AND SUBSYSTEMS DESIGN OPTIMIZATIONS	4
1.6 RESULTS AND DISCUSSION	7
2. EXERGY METHODS FOR THE INTEGRATED MISSION-LEVEL SYNTHESIS/DESIGN ANALYSIS AND OPTIMIZATION OF HYPERSONIC VEHICLES	17
2.1 INTRODUCTION	17
2.2 VEHICLE SUBSYSTEM AND COMPONENT MODELS	20
2.2.1 INLET MODEL	20
2.2.2 COMBUSTOR MODEL	22
2.2.3 NOZZLE MODEL	24
2.3 AIRFRAME SUBSYSTEM AERODYNAMIC/GEOMETRIC MODEL	26
2.3.1 LIFT, DRAG, AND FORCE ACCOUNTING MODEL	26
2.3.2 SUPPLEMENTAL LIFT AND TRIM MODEL	28
2.3.3 VECHICLE WEIGHT FRACTION MODEL	30
2.3.4 AIRFRAME SUBSYSTEM AERODYNAMIC LOSS MECHANISMS	30
2.3.5 AFS-A SOLUTION PROCEDURE	31
2.4 MISSION OVERVIEW	31
2.5 ANALYSIS AND OPTIMIZATION PROBLEM DEFINITIONS AND SOLUTION PROCEDURES	34
2.6 RESULTS AND DISCUSSIONS	36

2.6.1 VALIDATION RESULTS AND VEHICLE COMPONENT/SUBSYSTEM CHARACTERISTICS 37
2.6.2 EXERGY ANALYSIS RESULTS 44
2.6.3 EFFECTS OF SINGLE MISSION SEGMENT DISCRETIZATION 49
2.6.4 INTEGRATED MISSION SYNTHESIS/DESIGN OPTIMIZATION RESULTS 52
2.6.5 SINGLE MISSION SEGMENT SYNTHESIS/DESIGN OPTIMIZATION RESULTS 60
3. CONCLUSIONS 62
4. REFERENCES 64

1. INVESTIGATION OF THE EFFECTS OF DIFFERENT OBJECTIVE FUNCTIONS/FIGURES OF MERIT

1.1 INTRODUCTION

The growing complexity of aerospace systems has given rise to increased susceptibility to non-optimal performance as a result of improper integration of the synthesis/design and optimization of the components and subsystems. Therefore, a critical need exists for improved analysis and optimization methods for modeling, evaluating, and optimizing performance. Exergy-based synthesis/design analysis and optimization methodologies, which can relate every system component and subsystem to overall system requirements in a framework of common metrics, is reasonably mature for the synthesis/design analysis and optimization of stationary power and cogeneration as well as aero-engine component applications. It has also received a lot of attention lately as a potentially useful method for aircraft system/subsystem synthesis/design analysis and optimization (e.g., see [1-14]). The advantages of exergy-based methodologies for application to aircraft systems stem from their ability to support all required levels of synthesis/ design activity in a unified fashion, from conceptual comparisons through to the final configuration, leading to system-level, *best* or *optimized*[1] syntheses/designs. This approach can significantly streamline the analysis and optimization process for component/ subsystem/system synthesis/design, minimize ground-based testing, and substantially reduce certification time and costs.

A lot of very useful research over the last decade has been focused on how to apply exergy analysis to aircraft system synthesis/design and operation [6-13]. The advantages of doing so for stationary systems have been known since at least the 1960s. However, applying these same techniques, developed for and applied to stationary systems, to aerospace systems has required additional thought and work. In the applications which appear in [6-13], exergy-based methods are compared with typical energy-based ones for determining the synthesis/design and operational optimization of hypersonic and morphing and non-morphing vehicle systems and sub-systems (including the airframe). The advantages of using the former are clear.

As to the application of large-scale optimization to the synthesis/design of high performance aircraft, the success of the work found in [1-5] for highly non-linear, high fidelity models with a

[1] The adjective *best* is used here to describe the synthesis/design found purely through analysis and *optimum* to describe that found through mathematical optimization.

large number of degrees of freedom at the optimization level is to a large part due to the decomposition methods developed and used by the authors. However, it must be emphasized that even when very sophisticated methods of optimization and decomposition are successfully applied, care must be taken in formulating the overall objective function for the system. In other words, does it matter whether or not the objective function is energy based or exergy based? The answer at least from the standpoint of the work which will be presented here is that it depends on what system subsystems with degrees of freedom are included in the optimization process. For example, in [1], a number of different types of decomposition including iterative Local-Global Optimization (ILGO) are applied to the synthesis/design optimization of an advanced tactical aircraft (ATA) system with and without degrees of freedom (DOF) for the airframe subsystem (AFS-A). The ATA system is optimized using a total of 493 (for the case with AFS-A degrees of freedom) and 481 (for the case without AFS-A degrees of freedom) synthesis/ design and operational decision variables. When the optimum values of selected ATA AFS-A geometric variables for the case with and without AFS-A degrees of freedom are compared, the optimum vehicle, when AFS-A degrees of freedom are considered, is 6.3% lighter than the optimum vehicle without AFS-A degrees of freedom. Thus, adding these degrees of freedom improves the optimum found. However, since minimization of the W_{TO}, is equivalent to minimizing the fuel weight, the question posed is the optimum vehicle with AFS-A degrees of freedom equivalent to the minimization of energy consumption for the whole vehicle, i.e. can one do better by changing the objective function to one based on exergy instead of energy? The work presented in detail in the M.Sc. thesis work of Vijayanand Periannan entitled *Investigation of the Effects of Different Objective Functions/Figures of Merit on the Analysis and Optimization of High Performance Aircraft System Synthesis/Design* [9] and found on http://scholar.lib.vt.edu/theses/ tries to answer this question as well as show the usefulness of an exergy analysis in understanding how the losses in the system effect the final optimum outcome. What is presented in the remainder of this section, *Section 1*, is a brief description of the models developed and used for an Advanced Aircraft Fighter (AAF) in the above M.Sc. thesis, the optimization problems solved, and some of the results obtained. The AAF consists of a Propulsion Subsystem (PS), an Environmental Control Subsystem (ECS), and an Airframe Subsystem (AFS-A where the "-A" refers to the aerodynamics).

1.2 PROPULSION SUBSYSTEM (PS) MODELS

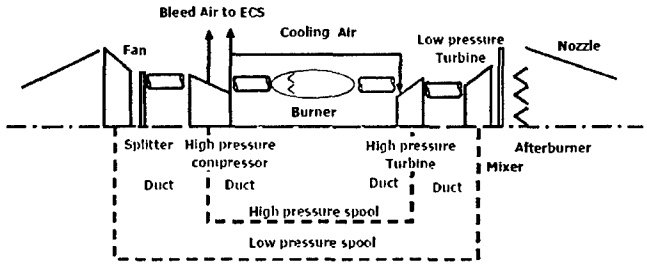

Figure 1. Turbofan engine components of the PS [9,5].

The schematic diagram of the two-spool, low-bypass, turbofan engine used as the basis for the PS is shown in Figure 1. Detailed descriptions of the physical (i.e. weight and dimensions), off-design, heat transfer, and thermodynamic models used for the PS are found in [9]. Turbine cooling is also incorporated into the engine analysis. Cooling air is drawn from the compressor exit with a portion used for cooling the high pressure turbine nozzle guide vanes and the remainder for cooling the high pressure turbine rotor. No cooling is included for the low pressure turbine.

The model of the engine uses non-dimensional compressor and turbine performance maps to find the efficiencies at off-design conditions as a function of mass flow rate and pressure ratio, while mass, momentum and energy balances are used to model the thermodynamic behavior of the various components inside the PS. The model provides the thermodynamic properties (pressure, temperature, etc.) at each of the engine stations, the inlet air flow rate, nozzle areas, and the fuel consumed in the combustor and afterburner adjusted to provide the thrust required during the different segments of the mission. Assumptions made are as follow: steady flow; 1D flow at the entry and exit of each component and at each axial station; fan driven by a low pressure turbine, which also provides the mechanical power for accessories; high pressure bleed air and cooling air removed at the end of the compressor; isentropic flow in the bypass duct; and completely mixed fan and core streams in the mixer.

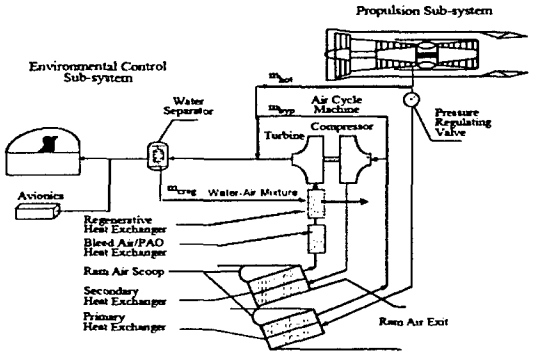

Figure 2. Schematic of an ECS bootstrap air cycle [9,5].

1.3 ENVIRONMENTAL CONTROL SUB-SYSTEM (ECS) MODELS

The ECS modeled here is a conventional bootstrap system which provides conditioned air to the cockpit and avionics. It is shown schematically in Figure 2. Air flow to the ECS is from pre-conditioned

bleed air. Flow into the ECS is varied by a pressure-modulating valve at the ECS inlet which also limits the maximum inlet pressure to the ECS's primary heat exchanger and bootstrap compressor. ECS performance is closely coupled with the PS and the aircraft flight conditions. Changes in the power settings cause changes in bleed air pressures and temperatures, which in turn affect the performance of the ECS. Detailed descriptions of the physical, geometric, heat transfer, and thermodynamic models for the ECS are given in [9,5].

1.4 AIRFRAME-AERODYNAMICS SUBSYSTEM (AFS-A) MODELS

The AFS-A shown in Figure 3 is defined as the empty aircraft, which includes fuselage, wings, tail, gear, etc. but excludes the fuel weight, the PS weight, the ECS weight, and the payload. A master equation for flight performance in terms of thrust loading (T_{SL}/W_{TO}) and wing loading (W_{TO}/S) is derived directly from energy considerations as a function of the storage of potential and kinetic energy, respectively, due to changes in altitude *(h)* and aircraft velocity *(u)*. If one assumes that the installed thrust is given by $T = \alpha T_{SL}$, where α is the installed full throttle thrust lapse, which depends on altitude and speed, and the instantaneous weight is given by $W = \beta W_{TO}$, where β depends on how much fuel has been consumed and how much payload has been delivered, the master equation for flight is given by

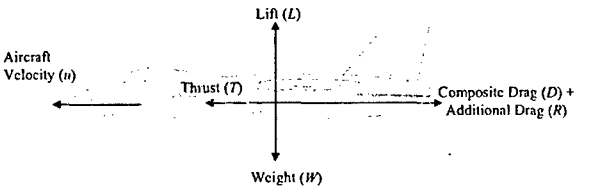

Figure 3. Force balance on the aircraft [9.5].

$$\frac{T_{SL}}{W_{TO}} = \frac{\beta}{\alpha}\left\{\left(\frac{D+R}{\beta W_{TO}}\right) + \frac{1}{u}\frac{d}{dt}\left(h + \frac{u^2}{2g}\right)\right\} \tag{1}$$

A complete description of the aerodynamic and geometric models for the AFS-A appears in [9,5].

1.5 SYSTEM AND SUBSYSTEMS DESIGN OPTIMIZATIONS

Five different optimization problems for the design of the AAF system are investigated and the results compared. They are defined in the sections below for the thirteen segment mission (warm-up, takeoff acceleration, takeoff rotation, accelerate, climb, subsonic cruise climb 1, combat air patrol, supersonic penetration, combat turn, combat acceleration, escape dash,

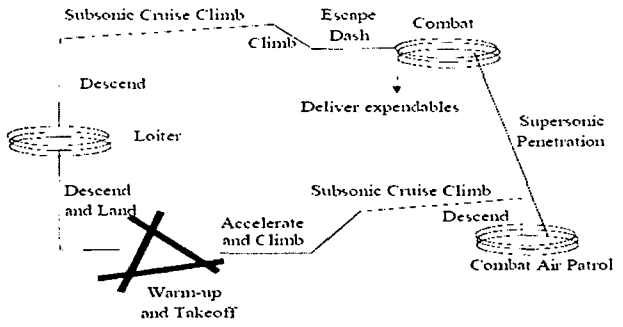

Figure 4. Schematic a the fourteen segment mission profile [9,5].

subsonic cruise climb 2, loiter) depicted schematically in Figure 4 [9,5]. The five objectives, each defining a different optimization problem are as follow:

1. Objective 1: minimization of the gross takeoff weight;
2. Objective 2: minimization of the total exergy destruction of the PS and ECS plus the total amount of unburned fuel exergy lost out the backend of the PS;
3. Objective 3: minimization of the total exergy destruction of the PS and ECS as well as the exergy destruction due to the frictional losses associated with the parasitic drag the AFS-A plus the total amount of unburned fuel exergy lost out the backend of the PS; note that in [6-8], the exergy destruction due to the induced drag is also included;
4. Objective 4: maximization of the thrust efficiency given by the ratio of the thrust work to the energy of the fuel used (both burned and unburned);
5. Objective 5: maximization of the thermodynamic effectiveness [15] given by the ratio of the thrust work to the maximum thrust work which the PS could provide were no irreversibilities present in the PS and ECS and were all the fuel delivered to the engine burned; note that this measure, of course, ignores the exergy destruction due to parasitic drag in the AFS-A and must be updated to reflect this additional destruction when the AFS-A is optimized (allowed degrees of freedom, i.e. decision variables) alongside the PS and ECS; this is in fact done in the last set of optimizations presented below.

Table 1. PS decision variables and inequality constraint limits [9].

Component	**Decision Variables**		**Constraints**
Fan	α	Fan bypass ratio	$0.1 \leq \alpha \leq 0.6$
	PR_{fan}	Fan design pressure ratio	$3 \leq PR_{fan} \leq 9$
Compressor	PR_{comp}	Compressor design pressure ratio	$4 \leq PR_{comp} \leq 10$
Afterburner	T_{aft}	Afterburner Temperature	$T_{aft} \leq 2000$
Component	**Operational Decision Variable**		**Constraints**
Turbine	T_B	Turbine inlet temperature	$T_B \leq 1778$

The design and operational decision variables used for the PS

Table 2. ECS decision variables and inequality constraint limits [9].

Component	Design Decision Variables		Constraints
Primary heat exchanger	L_c	Cold side length (m)	$0.06 < L_c < 0.9$
	L_h	Hot side length (m)	$0.5 < L_h < 0.9$
	L_n	Non flow length (m)	$0.5 < L_n < 0.9$
Bleed air / hot PAOS heat exchanger	L_c	Cold side length (m)	$0.06 < L_c < 0.9$
	L_h	Hot side length (m)	$0.5 < L_h < 0.9$
	L_n	Non flow length (m)	$0.5 < L_n < 0.9$
Air cycle machine	R_{cp}	Compressor design pressure ratio	$1.8 < PR_{cp} < 3.0$
Regenerative heat exchanger	L_c	Cold side length (m)	$0.15 < L_c < 0.3$
	L_h	Hot side length (m)	$0.3 < L_h < 0.5$
	L_n	Non flow length (m)	$0.3 < L_n < 0.5$
Component	**Operational Decision Variables**		**Constraints**
Pressure regulating valve	R_{vv}	Pressure setting	$PR_{vv} < 6.0$
Splitter	m_{byp}	Bypass air flow rate	$m_{byp} < 0.2$ kg/s

Table 3. AFS-A decision variable and constraint limit [9].

Design Decision Variable	constraint
W_{TO}/S	$65 < W_{TO}/S < 75$

are given in Table 1 along with their constraint limits, while those for the ECS are shown in Table 2. When degrees of freedom are included for the AFS-A, a single design decision variable is considered and appears in Table 3 along with its constraint limit.

The interdependence between the subsystems of the aircraft system is quite tight. For some of the optimizations, only the PS and ECS are allowed degrees of freedom yet the AFS-A does play a role, even if only a passive one in the process of design optimization. Thus, for this case, the ECS's optimal design is affected by the optimal design and operational decisions made in the PS and vice versa. Furthermore, when synthesis/design degrees of freedom are allowed for the AFS-A as they are in some of the optimizations performed here, the design decision of this subsystem influence the syntheses/designs of both the PS and ECS and vice versa. The result is that the AAF system represents the typical case of a system in which "everything influences everything else". Thus, determining the optimal synthesis/design of the aircraft system requires that the optimal synthesis/design of each of the aircraft subsystems (e.g., the PS, ECS, and AFS-A) be carried out in an integrated fashion. The alternative is that the individual subsystem optimizations do not lead to the optimum for the system as a whole.

Finally, gPROMS®, a dynamic development environment developed by PSE [16], is used both for modeling and flying the AAF system as well as optimizing its design. The non-linear programming solver (i.e. gradient-based optimization method) used is the SQRPD solver which is based on the sequential quadratic programming (SQP) algorithm.

1.6 RESULTS AND DISCUSSION

A parametric exergy analysis on the AAF vehicle is performed first with a focus on the PS to identify the behavior of some of the key system quantities (i.e. the rate of exergy destruction, specific thrust, and specific fuel consumption) with changes in the parameters which tend to influence them the most. These are the compressor pressure ratio, the fan bypass ratio, and the turbine inlet temperature. For complete details of this study, the reader is referred to [9]

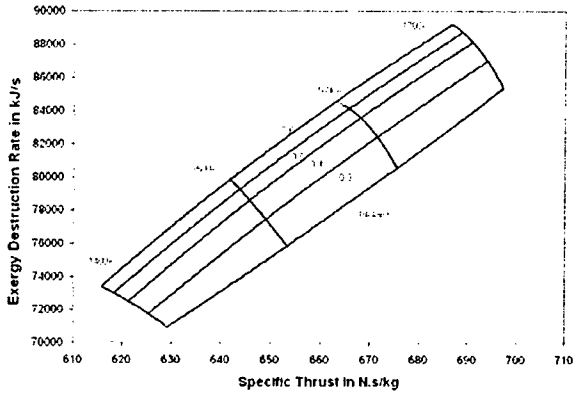

Figure 5. Variation for mission segments 1 and 2 (Warm-up/Takeoff Acceleration) of the vehicle exergy destruction rate with vehicle specific thrust, fan bypass ratio, and turbine inlet temperature for a fixed compressor pressure ratio of 8 [9].

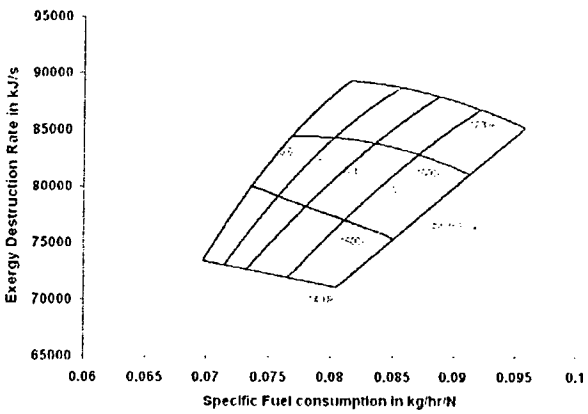

Figure 6. Variation for mission segments 1 and 2 (Warm-up/Takeoff Acceleration) of the vehicle exergy destruction rate with specific fuel consumption, fan bypass ratio, and turbine inlet temperature for a fixed compressor pressure ratio [9].

For mission segments 1 and 2 and a fixed compressor ratio of 8, the rate of exergy destruction is plotted versus specific thrust in Figure 5. The bypass ratio is varied over a range of 0.2 to 0.6 and the turbine inlet temperature is varied from 1400 K to 1700 K. As can be seen, the exergy destruction rate at this compressor pressure ratio and a given specific thrust decreases generally with decreasing by-pass ratio and turbine inlet temperature. Thus, the trade-off which exhibits itself is that changing the design of the PS towards lower by-pass ratios results in better, more efficient designs provided the turbine inlet temperature is decreased as well. Furthermore, there is a tendency for the by-pass ratio contours to bunch more towards the higher rates of exergy destruction for any given specific thrust. This, of course, implies that the effect of changes in by-

pass ratio at these rates is less than at lower values of the rate of exergy destruction in the vehicle.

The variation of the rate of exergy destruction with specific fuel consumption, fan bypass ratio and turbine inlet temperature for a fixed compressor ratio of 8 and for mission segments 1 and 2 is shown in Figure 6. The exergy destruction rate at fixed specific fuel consumption has a clear cut trend of decreasing with decreasing by-pass ratio and decreasing turbine inlet temperature. As before, the trade-off which exhibits itself is that changing the design of the PS towards lower by-pass ratios results in better more efficient designs provided the turbine inlet temperature is decreased as well.

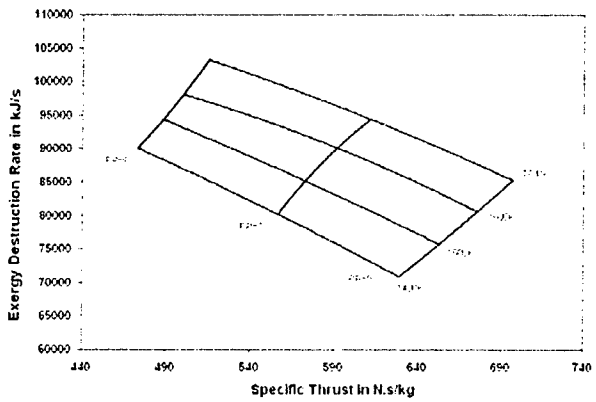

Figure 7. Variation for mission segments 1 and 2 (Warm-up/Takeoff Acceleration) of vehicle the exergy destruction rate with specific thrust, turbine inlet temperature, and compressor pressure ratio for a fixed bypass ratio of 0.2 [9].

For a fixed by-pass ratio of 0.2, the variation of the vehicle exergy destruction rate in segments 1 and 2 with specific thrust, turbine inlet temperature, and compressor pressure ratio are shown in Figure 7. As can be seen from this figure, the exergy destruction rate at this by-pass ratio and a given specific thrust decreases generally with increasing compressor pressure ratio and decreasing turbine inlet temperature. Another observation is that as the compressor pressure ratio increases, the variation of the exergy destruction rate and the specific thrust increases with variations in turbine inlet temperature.

Turning now to the optimization results, we first examine those for Objectives 1, 2, 4, and 5. Two of these are energy based and involve minimization of the total gross takeoff weight and maximization of the thrust efficiency. The other two are exergy based and involve minimization of the exergy destruction in the PS and ECS plus the exergy fuel loss out the backend of the engine and maximization of the thermodynamic effectiveness. For all four of these optimizations, the same set of decision variables is used. The optimum values of the design decision variables are given in Table 4. For these optimizations, a set of 4 design and 13 operational (1 per mission segment) decision variables for the PS and 10 design and 26 (2 per

mission segment) operational decision variables for the ECS are used. Thus, a total of 14 design and 39 operational decision variables for the AAF system optimization are employed. In this set of optimizations, no decision variables are allowed for the AFS-A.

In doing the optimization for each objective function, a set of two separate optimizations are done, i.e. a primary one and a secondary one. For the former, one mission segment, Takeoff Acceleration, which is the most constrained of all the segments, is chosen as the design-point segment. This segment is used to optimize the AAF system and each subsystem with respect to the design decision variables and the operational decision variables for that segment in order to determine an optimal set of values for the design decision variables which fix the geometric and thermodynamic characteristics[2] of the AAF system and its subsystems. Once these are fixed, the AAF and its subsystems are optimized in the secondary optimization with respect to the operational decision variables associated with each of the other twelve mission segments. It is the total weight and performance of the aircraft and its subsystems in all thirteen mission segments which determines the optimal value of each objective function reported here even though it is only the primary optimization of each objective which actually determines the optimal vehicle and subsystem. Of course, a more complete approach would be to optimize each objective with respect to the design and all of the operational decision variables simultaneously, but that is not done here for purposes of simplification since the goal of this work is a

Table 4. Optimum values for the design decision variables of the PS and ECS for the various objectives [9].

Subsystem		Objective Function			
		Minimize W_{TO}	**Minimize** $\dot{E}_{X_{obj.2}}$	**Maximize** η_{thrust}	**Maximize** ε_{thermo}
ECS Subsystem					
Cold-side length (m)	$L_{c\ (\text{Prim HX})}$	0.065	0.08	0.06618	0.05
Hot-side length (m)	$L_{h\ (\text{Prim HX})}$	0.55	0.6	0.4758	0.4
Non-flow length (m)	$L_{n\ (\text{Prim HX})}$	0.7	0.7	0.7	0.7
Cold-side length (m)	$L_{c\ (\text{Sec HX})}$	0.4	0.24	0.3052	0.2
Hot-side length (m)	$L_{h\ (\text{Sec HX})}$	0.45	0.35	0.5143	0.3
Non-flow length (m)	$L_{n\ (\text{Sec HX})}$	0.85	0.8	0.85	0.85
Compressor pressure ratio	PR_{cp}	2.2	2.0565	2.2	1.85084
Cold-side length (m)	$L_{c\ (\text{Reg HX})}$	0.2	0.2	0.2	0.26655
Hot-side length (m)	$L_{h\ (\text{Reg HX})}$	0.6	0.5	0.6497	0.3
Non-flow length (m)	$L_{n\ (\text{Reg HX})}$	0.2	0.3	0.2552	0.2
PS Subsystem					
Fan bypass ratio	α	0.3	0.350712	0.3	0.301149
Fan design pressure ratio	PR_{fan}	8.16759	8	8	8
Compressor pressure ratio	PR_{comp}	10.2095	10	10	9.9999
Afterburner temperature	T_{aft}	1223	1223	1223	1223

[2] Acrodynamic characteristics are also fixed at this stage but not optimally since for this particular set of optimizations the AFS-A are not permitted optimization degrees of freedom. For the next set of optimizations, these degrees of freedom are included.

comparison of optimal objectives and not a determination of some particular optimal vehicle per se.

Figures 8 to 10 provide a comparison of the objective function results. From Figure 8, it can clearly be seen that the results for the gross takeoff weight obtained from all four objective functions is similar. The percentage difference between the largest value and the smallest value among the four weights is less than about 1.5% and can be attributed to the optimization algorithm that was used. Similarly, from Figures 9 and 10, it can clearly be seen that the differences, in total fuel weight and the exergy destruction for the four different objective functions is negligible. Hence, it is concluded that all four objective functions predict the same optimum for the aircraft of minimum fuel consumption. The reason for this result for Objective 1 is that when minimizing the gross takeoff weight, the required thrust to fly the aircraft also reduces due to a lighter aircraft. This in turn reduces the thrust work required and hence less fuel energy is required to produce this work and, consequently, the fuel weight is reduced. As to minimizing the exergy destruction and fuel exergy lost out the backend of the vehicle (Objective 2), the less there is of both, the less fuel must be consumed to meet the vehicle demands to satisfy the mission requirements.

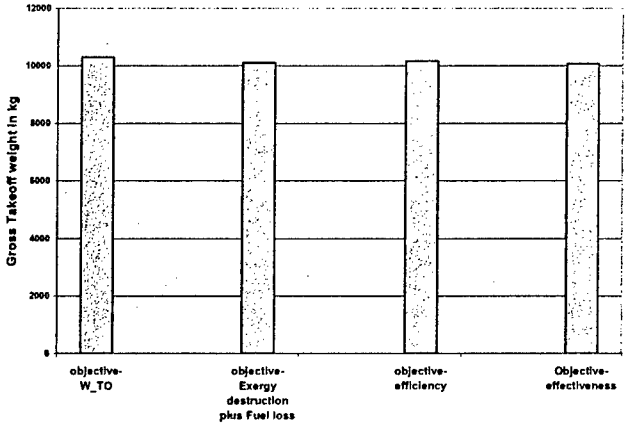

Figure 8. Comparison of the optimum gross takeoff weight obtained with four different objective functions/figures of merit, i.e. with objectives 1, 2, 4, and 5, respectively [9].

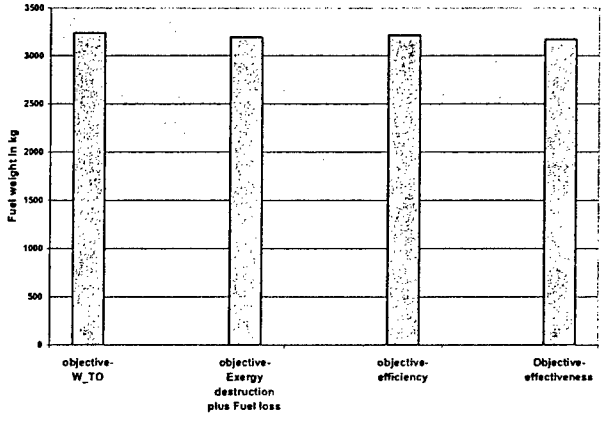

Figure 9. Comparison of the optimum fuel weight obtained with four different objective functions/figures of merit, i.e. with objectives 1, 2, 4, and 5, respectively [9].

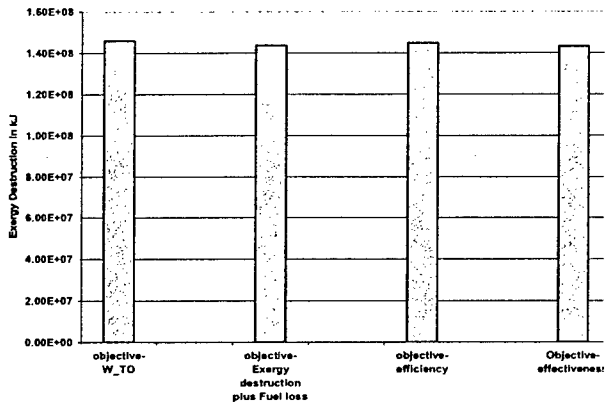

Figure 10. Comparison of the optimum exergy destruction obtained with four different objective functions/figures of merit, i.e. with objectives 1, 2, 4, and 5, respectively [9].

For Objective 4, the picture is more complicated in that in order to maximize the thrust efficiency, the denominator must be minimized which if the thrust power remains fixed is equivalent to minimizing fuel consumption since the denominator is the product of the mass flow rate and the lower heating value of the fuel. However, if the thrust power is not fixed, which is the case here, in addition to minimizing the denominator of Objective 4, one must maximize its numerator provided there are AFS-A degrees of freedom in play and/or the drag due to other subsystems such as the ECS (e.g., that due to its ram-air heat exchangers) is taken into account. This can be seen in our "master equation" above (equation (1)) where thrust depends on the parameters W_{TO}, D, and R, i.e. D is both the induced and parasitic drag of the AFS-A while R is the drag due to the ECS. Without AFS-A degrees of freedom, D is directly dependent on W_{TO}. Furthermore, R is very small compared to D and has little effect in this case on the thrust work. Thus, for our first set of optimizations here, maximizing the thrust efficiency (objective 3) effectively reduces to minimizing fuel consumption.

Finally, in the case of Objective 5, the role of the thrust work in the optimization is the same as that for Objective 4 which means that the maximization of Objective 5 reduces to that of minimizing Objective 2. However, as has already been argued, this leads to minimization of the fuel energy required.

It should be evident from the above that all four objectives (Objectives 1, 2, 4, and 5) do equally well when no AFS-A degrees of freedom are present and drag losses in other subsystems such as the ECS are small relative to those in the AFS-A. As is shown below, an additional consideration is whether or not the exergy losses due to drag and fuel loss in the AFS-A are included directly in the minimization or maximization of the objective. If in fact AFS-A optimization degrees of freedom are allowed and AFS-A irreversibilities minimized, as is done below and in [9] using Objective 3, the optimum vehicle found uses almost 10% and 6% less fuel without and with AFS-A degrees of freedom, respectively, than the optimum vehicle resulting

from a minimization of Objective 1. This is significant and is not simply attributable to the optimization algorithm used. Thus, the exergy-based objective appears in this case to be superior to all the other measures and provides a significant reason for using an exergy-based approach instead of one based-purely on energy.

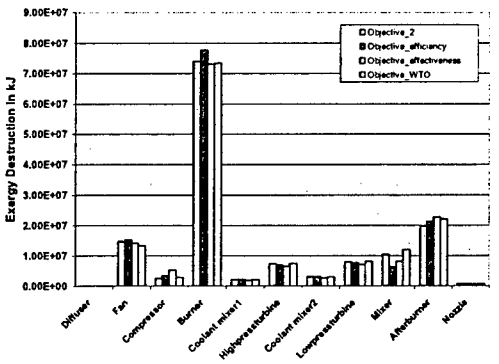

Figure 11. Optimal PS component exergy destructions for the entire mission [9].

Another reason to prefer an exergy-based approach is that the maps pinpointing internal losses characterized by the exergy destructions in each component of the PS and ECS fall directly out of the optimization process as seen in Figures 11 and 12. Coupled with performance plots such as the ones given in Figures 5 to 7, the designer is able to understand why the optimization has driven the vehicle design to the result produced and, furthermore, may lead to an even better result by allowing the designer to add optimization degrees of freedom at precisely those sites where the largest inefficiencies have been pinpointed by the exergy-based optimization. Such information is simply not available from a conventional energy-based approach.

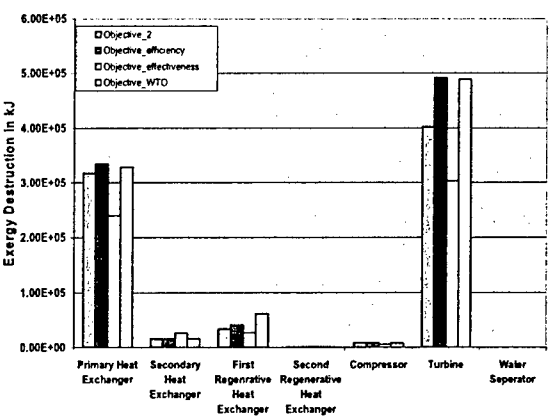

Figure 12. Optimal ECS component exergy destructions for the entire mission [9].

Figure 11 shows, for the four different objectives (Objectives 1, 2, 4, and 5), the total exergy destruction for the entire mission occurring in the components of the optimal PS, namely, the diffuser, fan, compressor, burner, coolant mixer 1, high pressure turbine, coolant mixer 2, low pressure turbine, mixer, afterburner, and nozzle. Figure 12 does likewise for the ECS. From these figures, it is obvious that the burner, afterburner, fan and the mixer in the PS are the components which contribute the most to the exergy destruction while the remaining PS components and those in the ECS contribute

significantly less to the total exergy destruction. Thus, based on the information given by these last two figures, the designer can add a new set of decision variables for a new round of optimizations which specifically affect the exergy losses in the burner, afterburner, and the mixer, reducing in the process the overall exergy destruction for the system even further.

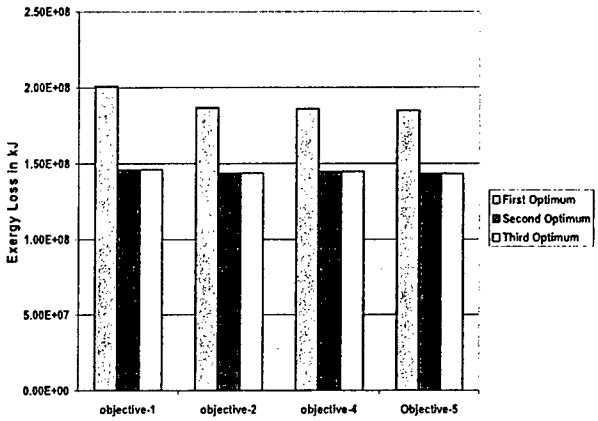

Figure 13. Exergy destruction obtained for objectives 1, 2, 4, and 5 and a series of three complete optimizations for each objective starting from significantly different initial points (1^{st}, 2^{nd}, 3^{rd}) [9].

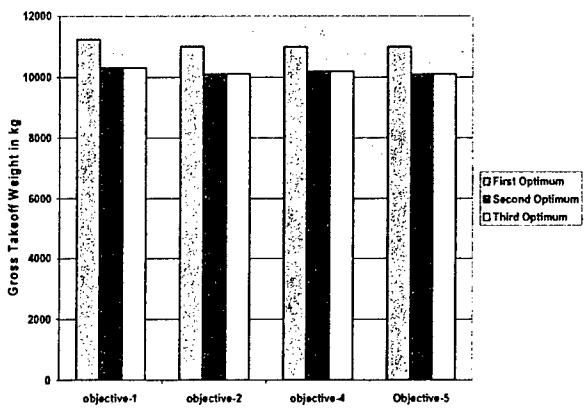

Figure 14. Gross takeoff weight obtained for objectives 1, 2, 4, and 5 and a series of three complete optimizations for each objective starting from significantly different initial points (1^{st}, 2^{nd}, 3^{rd}) [9].

The optimization results presented above for Objective Functions 1, 2, 4, and 5 were obtained using the gradient-based sequential quadratic programming (SQP) algorithm of gPROMS® [16]. However, gradient-based optimization algorithms have an inherent tendency to get stuck at local optimums depending, of course on the nature of the problem in question, i.e. its complexity, non-linearity, discontinuities, etc. In order to give some degree of confidence that the optimums found above are global instead of local, two additional rounds of optimizations are performed for the same four objective functions[3]. For these two new rounds, the initial guesses for the decision variables are made in such a way that they are significantly different from those used in the first round but within the same limits. This helps in determining if the algorithm has found a local optimum near the initial guess value or has indeed found the global optimum. From Figures 13 to 15, it is evident that the first round of

[3] This, of course, is not a guarantee of globality since satisfaction of the Kuhn-Tucker conditions would be required. However, to show that here would not be practical.

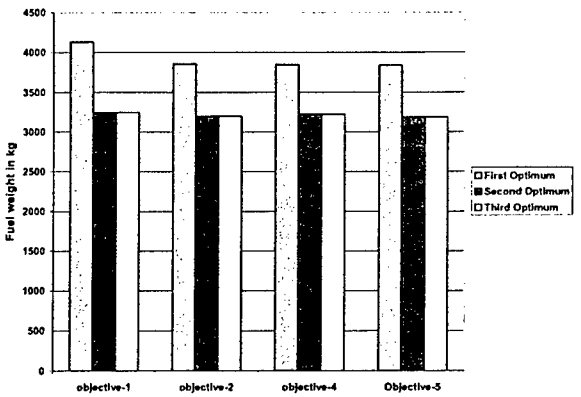

Figure 15. Fuel weight obtained for objectives 1, 2, 4, and 5 and a series of three complete optimizations for each objective starting from significantly different initial points (1^{st}, 2^{nd}, 3^{rd}) [9].

optimizations resulted in a local optimum while there is some confidence that the latter two rounds result in what is believed to be the global optimum.

Now, in order to study the effect of the AFS-A on the optimization, an AFS-A degree of freedom, the wing loading, (W_{TO}/S), is used and Objective 2 is replace with Objective 3. Wing loading is the ratio between the gross takeoff weight and the planform area (S). Included in the exergy-based objective (Objective 3) is the rate of exergy destruction due to airframe parasitic skin friction losses. Both Objectives 1 and 3 are optimized in order to compare the results obtained from a purely energy- as opposed to exergy-based objective.

An initial guess of 70 was assumed for W_{TO}/S for both objective functions. For the exergy-based (Objective 3) optimization, the optimal value of the W_{TO}/S was found to be 73.7. This is because with a higher wing loading, the planform area is less for a given gross takeoff weight and, hence, results in less exergy destruction in the AFS-A. For the energy-based (Objective 1) optimization, the optimal value was found to be 67.5. This is due to the fact that minimizing gross takeoff weight reduces W_{TO}/S without consideration for the exergy destruction occurring in the AFS-A, i.e. the AFS-A exergy destruction does not appear explicitly in Objective 1 as it does in Objective 3. Of course, to have confidence

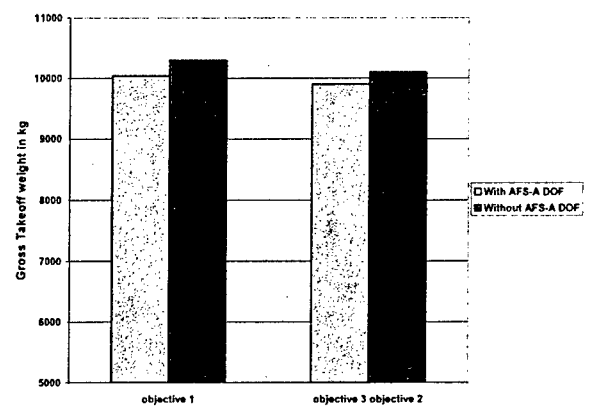

Figure 16. Optimum gross takeoff weight with and without AFS-A degrees of freedom for objectives 1, 2, and 3 where objective 1 is gross takeoff weight, objective 2 is exergy destruction plus exergy fuel loss excluding the exergy destruction in the AFS-A, and objective 3 is exergy destruction plus fuel exergy loss plus the exergy destruction in the AFS-A [9].

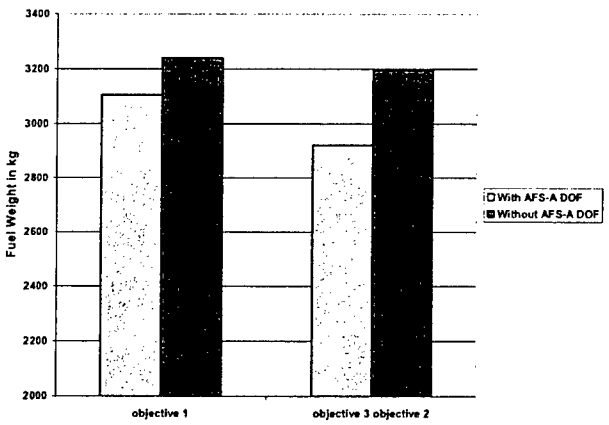

Figure 17. Optimum fuel weight with and without AFS-A degrees of freedom for objectives 1, 2, and 3 where objective 1 is gross takeoff weight, objective 2 is exergy destruction plus exergy fuel loss excluding the exergy destruction rate in the AFS-A, and objective 3 is exergy destruction plus fuel exergy loss plus the exergy destruction in the AFS-A [9].

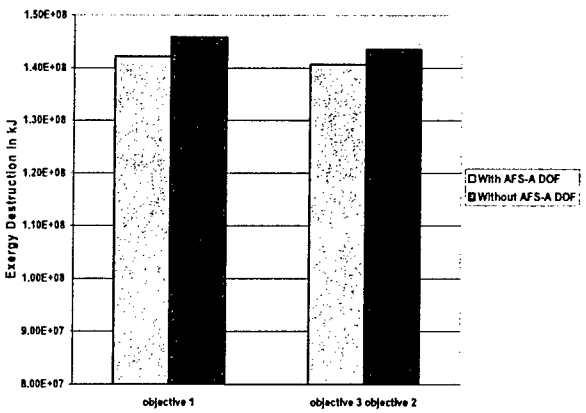

Figure 18. Optimum exergy destruction with and without AFS-A degrees of freedom for objectives 1, 2, and 3 where objective 1 is gross takeoff weight, objective 2 is exergy destruction plus exergy fuel loss excluding the exergy destruction in the AFS-A, and objective 3 is exergy destruction plus fuel exergy loss plus the exergy destruction in the AFS-A [9].

that the optimums found are global and not local, the optimizations were repeated twice more for both the objectives but with significantly different initial guesses for the AFS-A decision variable, i.e. with initial guesses for W_{TO}/S for both objectives starting significantly above the optimal value for W_{TO}/S (73.7) found for Objective 3 in the first optimization and significantly below the optimal value for W_{TO}/S (67.5) found for Objective 1 in its first optimization. The results confirm the conclusions given with respect to Figures 16 to 18 in the following.

Objective 3 includes the exergy destruction due to the parasitic skin friction in the AFS-A, along with the exergy destructions in the PS and ECS and the rate of exergy loss due to the fuel out the backend of the PS. The optimum value for this objective function is found to provide a better answer than the optimum solution obtained for Objective 2 when no degrees of freedom or parasitic losses for the AFS-A are considered. This can be seen in Figures 16 to 18. Figure 17 shows that the amount of fuel consumption has been reduced significantly, i.e. about 8.5%. Similarly, in Figures 16 and 18, it is evident that the optimization with Objective 3 and AFS-A degrees of freedom reduces the gross takeoff weight and the total exergy destruction as well.

In a comparison between the energy-based and exergy-based objectives (i.e. Objectives 1 and 3), the results given in Figures 16 to 18 show that the optimal solution obtained with the exergy-based objective (Objective 3) with AFS-A degrees of freedom is better than the one obtained with the gross takeoff weight as the objective (Objective 1) with and without AFS-A degrees of freedom - i.e. 5.8% and 9.8% less, respectively, than the total fuel consumption with the energy-based optimization with and without AFS-A degrees of freedom. The results confirm what was discussed earlier and point to the superiority of the exergy-based approach not only in terms of the detailed information provided on the locations and magnitudes of the inefficiencies present but also in terms of providing a better overall optimum vehicle.

2. EXERGY METHODS FOR THE INTEGRATED MISSION-LEVEL SYNTHESIS/DESIGN ANALYSIS AND OPTIMIZATION OF HYPERSONIC VEHICLES

2.1 INTRODUCTION

Air-breathing hypersonic vehicles hold the promise of approaching near-earth orbit. Using scramjets, i.e. supersonic combustion ramjets, as there means of propulsion for speeds exceeding five times the speed of sound, these aircraft offer performance capabilities previously only possible with rocket propulsion. Their principle advantage over the latter is that they need not carry their oxidant with them, which in rockets can easily approach or exceed 64% of the weight of the vehicle. Nonetheless, unique challenges await the developers of such aircraft, challenges which can only be met with the development of new analytical synthesis/design tools, materials, and test procedures capable of predicting and operating over a large range of pressures, temperatures, altitudes, and speeds.

Among the challenges which the designer faces is that at such high flight speeds aerodynamic integration of the scramjet engine is vital to the success of the vehicle; consequently, distinguishing airframe-engine boundaries becomes difficult. In fact, the entire lower surface of the aircraft can be considered the engine for the following reasons. For hypersonic flight at high altitudes, it is necessary to reduce drag. However, the low density of air requires a large compression surface (resulting in greater drag), and hence the forebody of the vehicle must be utilized as a diffuser. Similarly, nozzle areas greater than inlet areas are required to produce appreciable thrust. Thus, conventional axi-symmetric nozzles become large and impractical, and the afterbody surface must be used for free expansion. The resulting planar geometry introduces aerodynamic affects uncharacteristic of common aircraft. Pressures acting on the compression and expansion surfaces of the inlet and nozzle are greater than the ambient conditions, producing lift and introducing moments about the aircraft center of mass. This lift can potentially render wings obsolete and consequently, further reduces the ability to classify and investigate the engine and airframe separately.

In addition to the difficulty of distinguishing airframe-engine boundaries, the boundary between hypersonic and supersonic flows is also not well defined, although it is important to note that there is a distinct difference between the two flows, primarily resulting from the high

altitudes and high temperatures traversed in hypersonic flight. This difference leads to a number of unique challenges which must be effectively addressed. For example, thin shock layers and entropy layers characteristic of hypersonic flow provide unique challenges because they both interact with the boundary layer[4], essentially complicating analytical approaches. Viscous interactions occur where the thick boundary layer meets the outer inviscid flow, intensifying skin friction and heat transfer effects. In addition, these layers affect pressure distributions on the vehicle, thereby influencing lift, drag, and overall vehicle stability. High temperature effects result from viscous interactions by exciting and reacting molecules within the boundary layer, producing radiative heating. These effects can generate temperatures upwards of 11,000°K, making material selection critical [17]. In addition, convective or aerodynamic heating at hypersonic speeds can result in hydrogen embrittlement or oxidation of the structure [18]. Of particular significance to unmanned hypersonic vehicles, communications blackouts can result from ionized flows absorbing radio frequency radiation, making vehicle control another concern. Lastly, low density flows, rarely encountered in typical aerodynamic applications, further complicate design and analysis. These variations in flow properties at high altitudes require changes in conventional methods of analysis. For this situation particularly, continuum flow assumptions must be replaced by free molecule flow, greatly changing the governing equations and complicating analyses. Velocity slip, occurring when the viscous no-slip condition[5] fails, and temperature slip, occurring when the material surface temperature and gas surface temperature are unequal, result from low density flows as well.

Thus, both integration and modeling challenges are of particular importance with regards to hypersonic vehicle synthesis/design as is a lack of information about aerodynamic data and "rules of thumb" conventionally utilized in subsonic and supersonic vehicle synthesis/design, which complicates things even further. In addition, to address the high levels of system integration characteristic of hypersonic vehicle concepts, there is a need for a common metric such as *exergy* [15,19] capable of allowing the designer to more easily and clearly make performance trade-offs between sub-systems and a variety of phenomena. Of course, to achieve a high level of integration and an overall vehicle synthesis/design which is optimized requires optimizing all components and sub-systems simultaneously as demonstrated by, for example, Muñoz and von Spakovsky [3] and Rancruel and von Spakovsky [1,2,4] in their large-scale

[4] Shock layers merge with boundary layers while entropy layers introduce regions of strong vorticity within the boundary layer [17].
[5] The no-slip condition assumes that the flow velocity at the material surface is zero due to friction.

optimization of an advanced air fighter with 493 degrees of freedom over an entire mission. This becomes significantly more important the greater the need for an integrated synthesis/design there is; and, as will be shown, a separate and isolated approach to all aspects of hypersonic vehicle synthesis/design is not feasible. Of course, as also shown recently by, for example, Periannan [9], the choice of evaluation criteria (i.e. objective functions) utilized during the optimization not only affects the degree of integration and, therefore, the optimum vehicle found but the degree to which a designer is able to understand the integrations which are possible between the fundamentally different sub-systems and processes (e.g., the airframe aerodynamics and the engine propulsion).

In order to deal with this last issue of sub-system and process dissimilarities, a common measure or currency as mentioned above is needed [12]. Such a metric is *exergy*, which is a *non-conserved property* defined as the largest amount of energy that can be transferred from a system to a weight in a weight process while bringing the system to mutual stable equilibrium with a notional reservoir [12][6]. For example, airframe drag [20,6-9,21], inlet [22], engine [23,24,6-9,21], and environmental control sub-system [25,9,21] performance can all directly be measured on the basis of irreversibilities, which destroy or consume this non-conserved property called exergy. This is true for any other subsystem including the oil loop, hydraulic, electrical, fuel loop, and other subsystems which make up an aircraft. For a brief survey of the application of exergy methods and large-scale optimization with decomposition to the synthesis/design and operation of supersonic and hypersonic aircraft, the interested reader is referred to the M.Sc. thesis work of Markell entitled *Exergy Methods for the Generic Analysis and Optimization of Hypersonic Vehicle Concepts* [6] and to the M.Sc. thesis work of Brewer entitled *Exergy Methods for the Mission-Level Analysis and Optimization of Generic Hypersonic Vehicles* [7]. Both can be downloaded from http://scholar.lib.vt.edu/theses/. What is presented in the remainder of this section, *Section 2*, is a brief description of the models developed and used for a hypersonic vehicle in the above two M.Sc. theses, the optimization problems solved, and some of the results obtained. The hypersonic vehicle consists of a scramjet Propulsion Subsystem (PS) and an Airframe Subsystem (AFS-A, where the "-A" refers to the aerodynamics).

[6] Note that in the literature, the terms "availability" [19] and "generalized available energy" [15] are used synonymously with "exergy." This is true up to a point, but the more general of these concepts is the "generalized available energy" of Gyftopoulos and Beretta [15] which applies to all states (stable and not stable equilibrium) and includes the other two as special cases.

2.2 VEHICLE SUBSYSTEM AND COMPONENT MODELS[7]

2.2.1 INLET MODEL

A detailed description of the vehicle subsystem, component, and system models, solution procedures, and constraints used to simulate the hypersonic vehicles and hypersonic flight presented in this report are given in Markell [6] and Brewer [7]. In addition, both M.Sc. theses discuss other options for component modeling along with the benefits and shortcomings of each. The prevailing goal throughout component, subsystem and system development was to *accurately model flow behavior and loss mechanisms with the least possible computational burden.* Often, trade-offs between computational time and accuracy were made and were subsequently discussed.

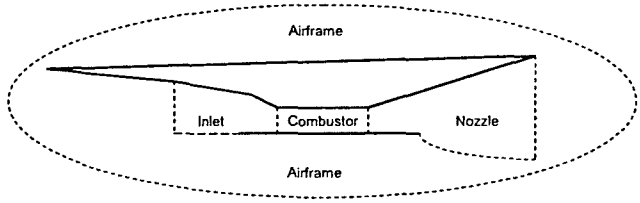

Figure 19. Propulsion sub-system components and airframe sub-system [7].

A breakdown of the hypersonic vehicle system can be seen in Figure 19. The propulsion subsystem (PS) consists of inlet, combustor and nozzle, while the airframe sub-system (AFS-A) guarantees the vehicle maintains force and trim balances throughout the varying flight conditions. The inlet plays a vital role in that small changes in inlet performance can greatly impact overall performance. One purpose of the inlet is to reduce the speed of the flow so that the majority of the fuel can be mixed with the incoming air and burned before leaving the combustor. A second is to compress the flow from conditions ahead of the vehicle to a temperature and pressure at which auto ignition of the fuel will occur. Flow uniformity at the combustor entrance is desired as well. From energy usage and performance standpoints, the inlet should perform these functions as efficiently as possible.

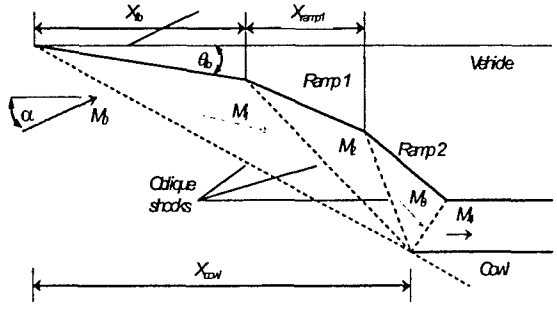

Figure 20. Inlet geometry and design details [6,7].

[7] All component and sub-system models were developed by Markell and Brewer in a joint effort to create an overall hypersonic vehicle simulation code [6,7].

The characteristics of the inlet's flow deceleration and compression are model via oblique shocks. As a result, a three-shock system geometry (see Figure 20) is chosen to satisfy the inlet performance needs. The three shocks, due to the forebody and first and second ramps, meet on the engine's cowl lip and a reflected shock intersects with the roof of the combustor entrance. It should be noted that technically, the forebody is not considered part of the inlet since the inlet is normally considered to start at the position of the first ramp. However, for force accounting purposes (see Brewer [7], Chapter 3), the forebody is included. Of course, in actuality, the forebody is considered an integral part of the diffusion process, and the high level of vehicle integration makes complete separation of the two components impossible. Here, the positions of the forebody, X_{fb}, the first ramp, X_{ramp1}, and the cowl, X_{cowl}, are referenced in the axial direction from the front of the vehicle. The forebody angle, θ_{fb}, is referenced to a line parallel with the vehicle centerline, and the angle of attack, α, is the angle at which the centerline of the vehicle is inclined to the direction of flight. A benefit of modeling the vehicle this way is that flow is delivered to the combustor aligned with the vehicle centerline which results in a streamthrust exiting the nozzle also aligned with the vehicle centerline. This greatly simplifies aerodynamic force and moment calculations.

Off-design for the inlet must also be addressed. All of the design decision variable values are fixed for each mission-level vehicle simulation so that, for example, there is no translating cowl capable of ensuring a shock-on-lip condition during varied flight conditions. Consequently, flow spillage[8] or shock ingestion calculations must be performed, or another method capable of maintaining shock-on-lip must be employed for off-design flight. The latter is chosen here based on the work of Moorhouse, Hoke, and Prendergast [22]. Here, energy exchange in the form of a heat interaction is required in front of the forebody oblique shock and the first inlet ramp shock. The conceptual system is shown in Figure 21. Heat is added or removed to bring the flight Mach number to the design Mach number, where the latter is the Mach number at which no energy interaction is needed for the

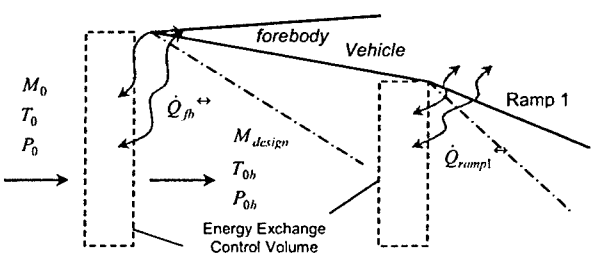

Figure 21. Inlet flow tailoring system using energy exchange [6,7].

[8] Flow spillage can be defined as the optimum mass flow minus the actual mass flow that enters the inlet at off-design operation.

forebody and first inlet ramp shocks to fall on the cowl lip, i.e. the combination of vehicle geometry and uninfluenced flight Mach number naturally locate the shocks-on-lip. As a result, the maximum mass flow is captured at each flight Mach number (each mission segment) at the cost of the energy interaction. The loss mechanism associated with this addition or removal of energy results in a loss due to irreversible heat exchange (i.e. across a finite temperature difference) and can be measured in terms of the rate at which exergy is destroyed. This rate of exergy destruction is not, however, charged to the inlet and, thus, the PS but to the AFS-A as are forebody friction and shocks. The two loss mechanisms in the inlet charged to the inlet and, thus, the PS are those due to friction and shocks and as with the energy addition are measured in terms of the rates of exergy destruction associated with each.

With an inlet design chosen for a given mission-level simulation, methods must be developed to find the resulting flow properties and model loss mechanisms within the component. A detailed solution procedure both for off-design and design developed by Markell [6] can be found in Markell [6] and Brewer [7].

2.2.2 COMBUSTOR MODEL

As to our next component in the PS, the combustor, a schematic of this component is given in Figure 22. As seen in this figure, the combustor has constant cross-sectional area fixed by the inlet geometry. In addition, it utilizes a mixing layer to incorporate incomplete combustion effects and captures heat transfer effects through the combustor wall (relative to preheating the fuel). The mixing layer represents the portion of the flow which has become "combustible," meaning adequate mixing of the air and fuel has occurred, enabling the chemical reaction. In addition, the mixing layer, and hence the exit flow, are assumed to be uniformly distributed across the area of the combustor. This assumption simplifies the analysis so that multiple streams, implying multiple energy, momentum, and conservation equations, need not be examined. The effects of ignoring multiple streams in one-dimensional flow are presented by Schindel [26], in which thrust losses of one percent can be expected. Schindel, however, performed this study at a fixed

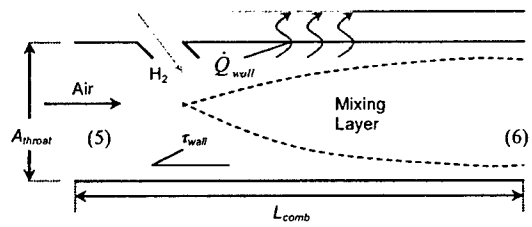

Figure 22. Combustor schematic [6,7].

angle of attack, in which case somewhat larger losses may result. Nonetheless, for the purposes of this analysis, acceptance of such a small error is deemed reasonable.

An additional assumption for the combustor model includes that of no dissociation due to the computational burden of solving finite rate kinetics. This is particularly important due to the large number of simulations require by the synthesis/design optimization process. However, with the constraints placed on the inlet and an analysis of the non-equilibrium and reaction rate chemistry of the constituents at the temperatures and pressures encountered in this study, Markell [6] demonstrates that this is a reasonable assumption. The air is modeled as twenty-one percent oxygen and seventy-nine percent nitrogen, and, thus, the resulting reaction mechanism governing the hydrogen-air interaction on a mole basis is given by

$$H_2 + a(O_2 + 3.76N_2) \rightarrow bH_2O + cO_2 + dH_2 + 3.76aN_2 \tag{2}$$

As a result, the stoichiometric fuel to air ratio is found to be $f_{st} = 0.0294$.

As to the solution procedure for the combustor, an explicit, differential marching scheme, as given in Markell [6], is used to find the variations in Mach number, temperature, pressure, and rates of exergy destruction due to irreversibilities (i.e. loss mechanisms) along the length of the combustor. These variations are found using the parameter values summarized in Table 5 [9] and the properties delivered to the combustor by the inlet, which as mentioned above, have already been constrained to provide sufficient conditions for combustion. The loss mechanisms include friction, heat transfer across a finite temperature difference, fuel/air mixing, and incomplete combustion. The sum of the rates of exergy destruction associated with these individual losses is the total loss attributed to the combustor.

Table 5. Combustor parameter values [7].

Parameter		Value
Skin friction coefficient, c_f		0.015
Hydrogen heat of reaction, h_{pr}		119,954 kJ/kg
Hydrogen Injection Data	Mach Number, M_{H2}	1.0
	Temperature, T_{H2}	600 °K
	Pressure, P_{H2}	101325 Pa
	Specific heat ratio, γ_{H2}	1.4
	Constant pressure specific heat, c_{pH2}	Constant
	Angle	45°

[9] The constant pressure specific heat is held constant during the injection process but may vary during each simulation based on the incoming flow properties.

2.2.3 NOZZLE MODEL

Frozen chemical equilibrium is assumed in the nozzle model so that the mole and mass fractions of the constituents from the combustor entering the nozzle are constant throughout the length of the nozzle. A schematic of the nozzle is presented in Figure 23. The products of combustion enter at position "6" and exit at position "7". As in the combustor, heat transfer and friction affect the flow through the nozzle.

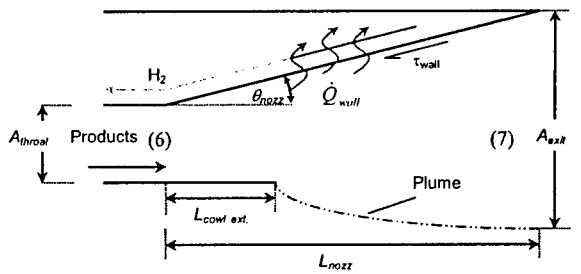

Figure 23. Nozzle schematic [7].

Two variables of particular importance to the nozzle are the nozzle expansion angle and the percentage the cowl extension. The former determines what value of area relief per unit length is provided to the flow by the free expansion surface and is fixed to fall between 8 and 18 degrees. Below 8 degrees, the nozzle does not produce any appreciable thrust; and, above 18 degrees, experimental results reveal operating conditions which deviate from predicted values [27]. The latter variable in one-dimensional flow impacts the force and moment imparted on the vehicle by the pressure inside the nozzle. In addition, the cowl length (see Figure 23) affects the position at which the *plume* starts. This length is chosen as a percentage of nozzle length because the latter varies, and the cowl extension rarely exceeds twenty-five percent of the nozzle length of hypersonic vehicle concepts due to cooling and weight restrictions [28,29]. Furthermore, although the length of the nozzle can vary, it is not an independent (decision) variable because the total vehicle length is assumed fixed, and since the inlet and combustor lengths vary, they dictate the nozzle length.

As with the combustor, a differential marching scheme is used to calculate the flow properties in the nozzle. This one, however, is provided by Shapiro [30]. In addition, unlike the combustor, mass is no longer being added and area change must be taken into account. Furthermore, loss mechanisms leading directly to rates of exergy destruction in the nozzle are those due to friction and heat transfer. Because the plume boundary is essentially imaginary, the losses associated with the shock/expansion process and drag associated with the increased exhaust area are drastically smaller than if a physical boundary were present and, thus, their contributions are neglected [31].

As a final note on the model for the nozzle, a two-dimensional program was initially developed to model the flow in the nozzle using the method of characteristics [32]. The goal of undertaking this approach began while trying to understand why the undersurfaces of many conceptual vehicles are curved [5]. This method is often used to calculate axi-symmetric nozzle contours and can do the same for free expansion scramjets. Shown in Figure 24, multiple characteristic lines, or Mach waves, as was discussed with regard to Prandtl-Meyer expansions, are drawn to accurately describe the flow direction and Mach number in each region between the lines. In essence, in two-dimensional flow, the Prandtl-Meyer equations are assigned a finite length for which they are valid. They are utilized to model the initial fan, and the reflections of that fan off the cowl surface determine many interesting nozzle attributes. The upper surface contour is shaped based on the cancellation of reflecting waves, i.e. a flat nozzle surface would yield undesirable reflections, whereas the curved surface in the figure is contoured necessarily to cancel these reflecting waves. For example, in the figure above, the ideal cowl length, i.e. the length at which the last fan is reflected, is roughly 3.3 meters of an assumed eight meter nozzle. Eight meters is not necessarily the ideal length, since an extended length could provide more vehicle lift. It is simply the length needed to correct the final expansion wave and align the flow to the axial direction. In addition, in actuality, the maximum cowl extension length that can be used for the vehicle is often limited by its overall weight and the ability to cool it [31].

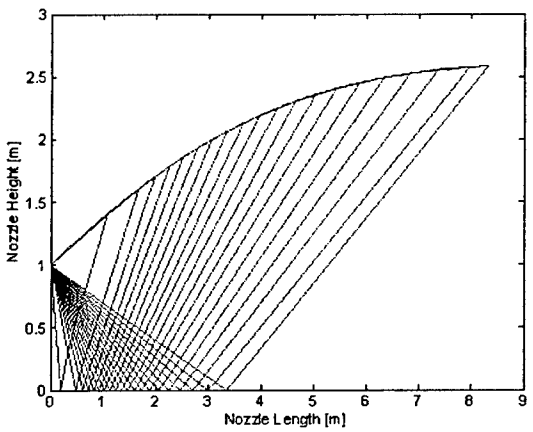

Figure 24. 2D method of characteristics applied to a nozzle with 25° nozzle entrance expansion angle and 1 meter throat height [7].

Unfortunately, this 2D model requires too much computational time when considered in light of the computational burden associated with the synthesis/design optimization process. It, thus, had to be abandoned and was replaced with the 1D model described in detail in Brewer [7]. In addition, the method of characteristics is based on irrotational, isentropic flow and, thus, must be modified from its current form to include heat transfer and frictional effects (loss

mechanisms). This technique is also employed for the design of isentropic inlets, and thus, a curved forebody and inlet geometry would result.

2.3 AIRFRAME SUBSYSTEM AERODYNAMIC/GEOMETRIC MODEL

The primary purpose of the AFS-A is to guarantee that forces and moments on the aircraft are balanced throughout the entire mission. As a result, models are developed to do a detailed force accounting and to calculate the center of mass, lift, and drag in order to guarantee steady and level flight. Figure 25 shows the forces acting on a hypersonic vehicle at a flight path angle of θ. These forces are the thrust, T, drag, D, lift, L, and weight, W. The drag acts along the direction of vehicle velocity, V, while the lift is perpendicular. The thrust acts along the vehicle centerline. The vehicle weight of course, equal to the mass multiplied by the gravitational constant, always acts in the downward vertical direction. The angle of attack, α, is the angle at which the vehicle centerline is aligned to the direction of the velocity. Both the angle of attack and the flight path angle are greatly exaggerated in the figure. Combined they do not exceed five degrees in this study because of the sensitivity of the inlet shock tailoring system.

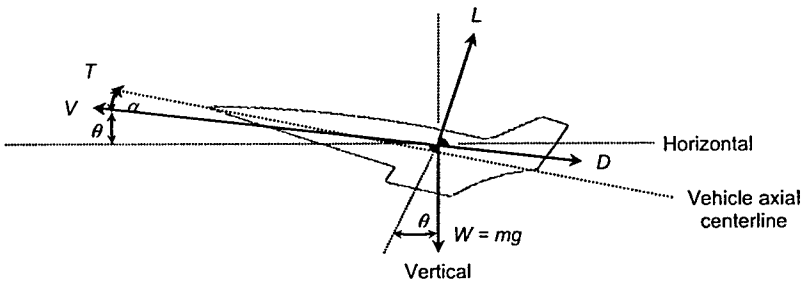

Figure 25. Forces acting on an aerospace vehicle during flight [7].

2.3.1 LIFT, DRAG, AND FORCE ACCOUNTING MODEL

A great deal of analysis is required to calculate the lift and drag of a hypersonic vehicle, particularly because at such high speeds the integrated vehicle fuselage/engine itself provides lift. This is quite different from conventional aircraft in which the majority of the lift is attributed to the wings. Thus, force accounting, or resolving all of the forces on the vehicle, is necessary to compute the required thrust and lift for the aircraft to perform its mission.

Various methods of force accounting in hypersonic propulsion are discussed in the literature [33,34]. The goal of each of these is to ensure that all forces acting on the vehicle are taken into account, and none is counted multiple times. Typically, the vehicle forces due to streamthrust, pressure, and friction are charged either to the PS or AFS-A, the division of which is represented

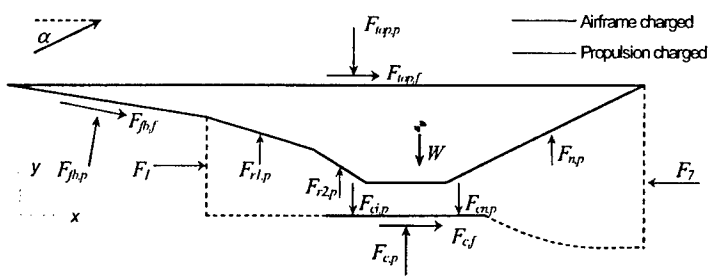

Figure 26. Resolved force accounting [7].

by the dotted line in Figure 26, where the x-component is considered parallel to the vehicle axialcenterline, and the y-component is perpendicular. If the forces under consideration are charged to the airframe, they are resolved into x and y-components. If they are charged to the propulsion sub-system, only the y-component is considered, and the x-component is assumed taken into account by the streamthrusts, F_1 and F_7 in the figure below. The choice of sub-system interface in this study only affects the assumption stated above.

All of the forces shown in Figure 26, except for the nozzle pressure force, $F_{n,p}$, are assumed to act at the center of their respective locations. For example, while the pressure force due to the forebody, $F_{fb,p}$, acts along the entire forebody surface, a net force is assumed to act at the midpoint of the forebody in the direction normal to the surface. This assumption simplifies the force and moment balance equations. The nozzle is a special case because the pressure along its length varies, and thus its pressure forces and moment contributions are calculated at each differential step.

The friction coefficient is assumed to be 0.001 for all surfaces [31]. For a one-dimensional approach, the surface area associated with the pressure and friction forces reduces to the length of the vehicle, while the area for the streamthrust force reduces to the height of the cross-section. With all of the properties known from the solution of each of the propulsion components, a force balance can be performed on the overall system. Thus, for a given mission segment, all of the forces acting on the vehicle are known. To maintain level flight, however, the moments about the vehicle center of gravity must be considered as well. As a result, the calculation of the vehicle's center of mass is essential. To this, one must, of course, determine the volume and the weight of the vehicle. Because of how the synthesis/design optimization problem is defined here, the empty weight of the vehicle is fixed while the volume is dependent on the optimization process. Essentially, the design decision variables dictate the geometry of the vehicle, and whatever the volume of that geometry compared to a baseline value results in a proportional weight density. Additional weight is dependent on the amount of fuel necessary to accomplish

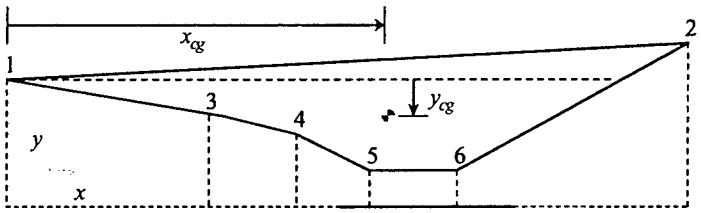

Figure 27. Illustration of integration technique [6,7].

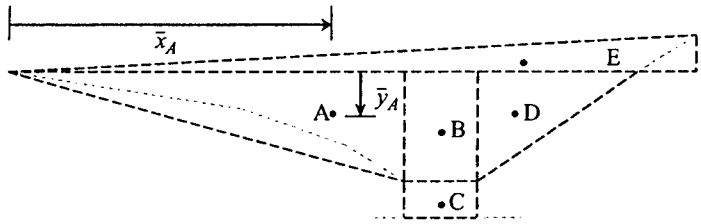

Figure 28. The five composite areas of the vehicle [6].

all mission segments and is discussed in the next section. The vehicle volume is specifically calculated by integrating the individual line segments of the vehicle geometry and adding and subtracting necessary values as illustrated in Figure 27.

As a final step in calculating the center of mass, the centroid of the vehicle, which corresponds to the center of gravity because a uniform constant density is assumed, must be determined. This is done using the *method of composite areas* [6] by breaking the body into five simple shapes, either rectangles or triangles, whose centroids are easily calculated and the sum of which approximately comprise that of the vehicle as illustrated in Figure 28.

2.3.2 SUPPLEMENTAL LIFT AND TRIM MODEL

To supplement the lift of the vehicle as well as trim the moment about the center of gravity, a wing, positioned at the center of gravity, and an elevon, positioned at the rear of the vehicle, are utilized as shown in Figure 29a. To correctly model the amount of lift available from a reference area, S, the lift and drag coefficients must be known and are given by

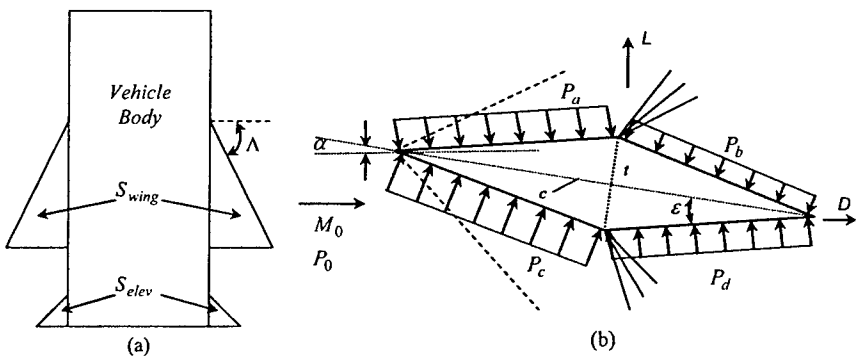

Figure 29. (a) Vehicle plan area and (b) elevon and wing cross-section detail [6,7].

$$C_L = \frac{2l}{\gamma M_0^2 c}\left(\frac{P_c - P_b}{P_0}\cos(\alpha+\varepsilon)+\frac{P_d - P_a}{P_0}\cos(\alpha-\varepsilon)\right) \tag{3}$$

$$C_D = \frac{2l}{\gamma M_0^2 c}\left(\frac{P_c - P_b}{P_0}\sin(\alpha+\varepsilon)+\frac{P_d - P_a}{P_0}\sin(\alpha-\varepsilon)\right) \tag{4}$$

The geometry chosen for S is a diamond airfoil shaped simple delta wing as illustrated in Figure 29b. Using two-dimensional shock-expansion theory on the assumed inviscid geometry, the values of pressure at each surface are known for any angle of attack, given a thickness to chord ratio, *t/c*. For this analysis, a fixed thickness to chord ratio of five percent is assumed, while the maximum thickness occurs at half of the total chord length of the airfoil. A detailed examination of this procedure is described by Anderson [35]. In actuality, the Mach numbers encountered by the wing would be less than freestream conditions due to the assumed blunt leading edge bow shock that occurs from the vehicle having some finite width. However, since a detached shock calculation is much more involved and only the one-dimensional aspects are of concern in this study, it is assumed that the Mach numbers encountered by the wing and elevon are equal to the freestream. Bow shock concerns are addressed by the constraints.

The wing is assumed fixed on the vehicle at zero angle of attack with respect to the vehicle centerline. Thus, a positive flight angle of attack is necessary to generate lift from the wings. As various amounts of lift are required from the wings during different mission segments, and since the airframe itself without wings is capable of generating lift, the wing area is allowed to vary from mission segment to segment. In addition, the center of pressure of the wing is assumed to act through the center of gravity of the vehicle so as to induce no moment.

As to the elevon, it must provide a moment equal and opposite to the vehicle moment; otherwise, the vehicle may pitch uncontrollably about its center of gravity. This is accomplished by assigning an area to the elevon, fixing its axial location, and inclining or declining it until the force necessary to cancel the moment is found. The elevon's area is determined from a relationship given in Bowcutt [36] and repeated in Brewer [7] and Markell [6] while its volume is assumed to be 0.04 [36]. The axial location of the elevon is one meter from the aft end of the vehicle, at a height equal to that of the nozzle free expansion surface. Allowing the angle of incidence of the elevon to vary both upward and downward, forces can be generated to cancel the vehicle moment and ensure stable flight.

2.3.3 VECHICLE WEIGHT FRACTION MODEL

The estimated empty vehicle mass is based on several prospective hypersonic vehicles as given in Curran and Murthy [28]. The empty mass of the vehicle is selected to be 5000 kg based on an estimated vehicle volume of 25 m^3 (with unit width). The takeoff[10] weight of the vehicle is assumed to be the sum of the empty mass and the fuel mass multiplied by the gravitational constant. In order to estimate the takeoff vehicle mass, fuel consumption over the mission must be estimated. The fuel mass fraction for each mission segment, a fraction of overall vehicle mass, is estimated by

$$\pi_f = \frac{m_{initial} - m_{final}}{m_{initial}} = 1 - \frac{m_{final}}{m_{initial}} \tag{5}$$

where $m_{initial}$ and m_{final} are the masses of fuel initially and finally for each mission segment. Of course, how the mass changes from the beginning to the end of the mission varies depending on the type of constraints imposed in each mission segment, i.e. cruise, acceleration, etc. Estimating the takeoff fuel mass is accomplished by examining each mission segment and relating the sum of the fuel mass fractions of each mission segment to the empty mass by

$$m_{takeoff} = \frac{m_{empty}}{\left(1 - \sum \pi_f\right)} \tag{6}$$

Thus, an initial mass can be estimated. More specifics about the calculation of the mass fractions due to each of the vehicle constraints can be found in Markell [6] and Brewer [7].

2.3.4 AIRFRAME SUBSYSTEM AERODYNAMIC LOSS MECHANISMS

The three primary loss mechanisms leading to exergy destruction in the AFS-A are due to friction, shocks, and energy addition across a finite temperature difference to maintain a shock-on-lip operating condition. The last of these was discussed above in *Section 2.2* on the PS. Losses due to shocks result from oblique shocks which occur at the forebody, external cowl, top surface, and tail. Frictional losses occur along these surfaces as well. No penalty is associated with morphing the wing and pitching the elevon, as it is assumed that the related irreversibilites

[10] "Takeoff" weight refers to the vehicle's maximum weight (i.e. before any fuel begins to burn during the first mission segment) when the hypersonic vehicle is launched at Mach 6. This varies from the traditional use of the term where the first mission segment is when an aircraft literally takes off from a runway.

(i.e. rates of exergy destruction) are small compared to the friction and shock contributions of the rest of the AFS-A.

2.3.5 AFS-A SOLUTION PROCEDURE

A detailed solution procedure for the AFS-A model is given in Brewer [7] and in Markell [6]. All of this can be accomplished within a reasonable set of constraints guaranteeing that flight is possible. As a result, the variables for the AFS-A are those given in Table 6, each of the dependent ones being a function of the angle of attack, α. It should be noted that all of the models presented previously are for a single angle of attack, which may or may not result in a "best" vehicle configuration. Therefore, both the PS and AFS-A must be iteratively solved though a range of angles of attack to ensure that a "best" configuration emerges. How this "best" configuration is defined, as well as the propulsive and aerodynamic requirements of thrust and lift for acceleration, climb, and turn mission segments are discussed below.

Table 6. AFS-A decision (independent) and dependent variables [7].

Variable	Classification	Symbol	Imposed Limits
Angle of Attack [°]	Independent, operational	α	$0.1 \leq \theta_{fb} \leq 6$
Wing planform area [m^2]	Dependent, operational	S_{wing}	$0 \leq S_{wing} \leq 0.10\, S_{veh}$
Elevon deflection angle [°]	Dependent, operational	ω	$0 \leq \omega \leq \omega_{max}$
Off-design forebody energy addition [kW] (see Figure 21)	Dependent, operational	$\dot{Q}_{fb}^{\leftrightarrow}$	Shock-on-lip
Off-design ramp 1 energy addition [kW] (see Figure 21)	Dependent, operational	$\dot{Q}_{r1}^{\leftrightarrow}$	Shock-on-lip

2.4 MISSION OVERVIEW

A scramjet vehicle mission is chosen based on the following two principal factors: the mission's potential as a future military application and the ability of the highly integrated vehicle to operate over the range selected. Keeping these aspects in mind, the following mission illustrated in Figure 30 developed with the assistance of Moorhouse [37] is used for the synthesis/design exergy analysis and optimization presented here. The total mission consists of six segments, shown in blue, with a payload operation assumed to occur during the fifth mission segment. As illustrated, scramjet operation begins at Mach 6. This necessarily assumes an initial stage (or stages) of propulsion (e.g., turbojet and ramjet) not specifically addressed in this

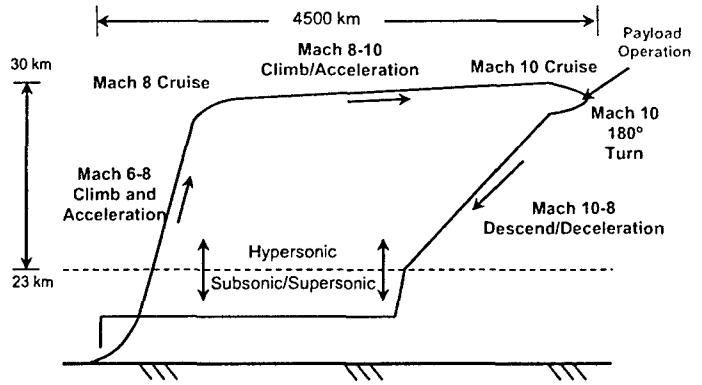

Figure 30. Total scramjet vehicle mission [6,7].

Table 7. Mission segment details [6,7].

Segment	Description
1	Accelerate and climb from Mach 6 (at 23.2km) to Mach 8 (at 26.9km), t = 90s
2	Mach 8 cruise for 600s
3	Accelerate and climb from Mach 8 (at 26.9km) to Mach 10 (at 30.0km), t = 90s
4	Mach 10 cruise for 600s
5	Perform a 180°, 2g sustained turn at Mach 10
6	Descend and decelerate to Mach 6

research. During each segment, the mass of the vehicle is considered constant. In essence, the thrust requirements are based on the initial mass at the beginning of each segment, and that thrust is sustained throughout the duration of the segment. In actuality, of course, the mass of the vehicle is constantly changing due to the consumption of the fuel, and consequently the vehicle performance requirements change as well. The consequences of such an assumption are addressed in the results chapter of Brewer [7].

The constraints for these segments as well as their general details are shown in Table 7 while the properties of air at altitude and the necessary velocities associated with maintaining a constant dynamic pressure of 85kPa are specified in Table 8. Depending on the desired performance criterion, the associated dependent ranges (R), times (t_{ms}), fuel mass fractions (π_f), changes in altitude (Δh) and velocity (ΔV), and load factors (n) must be established for each mission segment. These can be associated with flight along a constant dynamic pressure as described by Markell [6].

Table 8. Air and vehicle flight envelope data for a dynamic pressure of 85kPa [6,7].

Mach Number	6	7	8	9	10
Temperature [°K]	219.8	221.8	223.5	225.1	226.5
Pressure [Pa]	3378	2475	1901	1502	1204
Density [kg/m^3]	0.0533	0.0387	0.0295	0.0231	0.0184
Velocity [m/s]	1787	2094	2403	2712	3023
Altitude [km]	23.18	25.20	26.93	28.51	29.96

Table 9. Mission segment characteristics and constraining conditions [7].

No.	Mission Segment	t_{ms} [s]	T_{veh}-D_{veh} [kN]	θ[°] (see Figure 25)	R [km]	Δh [km]	ΔV [m/s]	π_f[1]	n
0	Mach 6-8 Acceleration	90	43.47	1.14	189	3.75	616	0.0521	1
1	Mach 8 Cruise	600	0	0	1442	0	0	0.0651	1
2	Mach 8-10 Acceleration	90	36.73	0.71	244	3.03	620	0.0508	1
3	Mach 10 Cruise	600	0	0	1814	0	0	0.0812	1
4	Mach 10 Turn	559	0	0	1690	0	0	0.0759	2
5	Mach 10-8 Deceleration	533	-6.075	-0.12	1447	-3.03	-620	0.0300*	1
	TOTALS	**2472**	-	-	**6826**	-	-	**0.3551**	-

*Based on program experimentation.

Details of how to determine these and the associated net thrust (or thrust minus drag: T_{veh}-D_{veh}) required for each specific mission segment are given in Brewer [7]. The specific values resul-ting from this determination are given in Table 9 for each of the six mission segments. These values are based on time and constant dynamic pressure constraints.

Finally, the total mission covers nearly 7000 km in roughly 41 minutes. How suitable these initial guesses for fuel mass fraction (π_f) are (they, in fact, are) is discussed in Brewer [7]. With the total mass fraction listed above and equation (6), the total takeoff mass of the vehicle is found to be 14080 kg. It can be seen that though the inclination angles for acceleration and deceleration mission segments are very small, the speed of the vehicle at each segment's respective Mach number allows for the completion of the segment requirements within the desired time frame. This implies that vehicle control in actual flight, i.e. maintaining a constant dynamic pressure, will indeed be challenging. With conventional aircraft, decelerations can be accomplished with negligible fuel use. However, the hypersonic vehicle must necessarily be constrained, for the geometry selected in this research, to only allow angles of attack greater than the forebody angle. If this constraint is ignored, undesirable expansions can occur in the inlet. Thus, a fuel mass fraction of 0.03 for the deceleration segment is selected based on preliminary runs of the program. The long range required for the turn is a consequence of selecting a small n (load factor, i.e. multiple of the vehicle weight the total vehicle lift must provide in order to accomplish the turn) value. As the vehicle is extremely sensitive to changes in flight conditions, a value of two was selected.

2.5 ANALYSIS AND OPTIMIZATION PROBLEM DEFINITIONS AND SOLUTION PROCEDURES

Multiple and distinct synthesis/design optimization problems are defined and solved in Markell [6] and Brewer [7]. Three of particular interest are the three developed for integrated mission-level synthesis/design analysis and optimization in Brewer [7]. These along with a limited set of results are presented here in this report. The interested reader can find the complete set of problems and results in Markell [6] and Brewer [7].

For the three optimization problems presented here, the most desirable vehicle is the one which can accomplish the entire mission using the least amount of fuel, starting with the same takeoff weight, i.e. empty weight, fuel weight, and payload. The objective of the first problem is the maximization of the vehicle's average thrust efficiency[11] weighted over the entire mission, a typical first law-based efficiency used as an evaluation criterion for vehicle synthesis/design. The objective of the second problem is the minimization of fuel weight over the entire mission while that of the third problem is the minimization of the total exergy destruction for the vehicle over the entire mission plus the exergy of the unmixed fuel mass (if any) that exits the combustor and is lost out the backend of the vehicle. The advantage of this exergy-based problem is that it can provide detailed information about the tradeoffs being made among the vehicle components and subsystems. An illustration of such tradeoffs via an exergy analysis is given in the *Section 2.6*.

As to the set of design and operational decision variables as well as the equality and inequality constraints for each of the optimization problems, they are the same for all three problems. The equality constraints are the model equations described in general terms above and in detail in Markell [6] and Brewer [7]. The inequality constraints are also given in these references and include those placed on the design and operational decision variables for the vehicle which appear in Table 10. Each problem has a total of 7 design decision variables and 6 operational decision variables. The latter are the angles of attack required for optimal operation in each segment of the mission. The former reflect geometric variables (i.e. lengths and angles) which define the vehicle shape and, at the optimum point, define the optimal shape of the entire vehicle, i.e. the airframe, inlet, combustor, and nozzle.

[11] The thrust efficiency η is also referred to in the literature as the overall efficiency or the product of the thermal and propulsive efficiencies, i.e. $\eta = \eta_{th}\eta_p$ where $\eta_{th} = \dot{KE}/\dot{m}_f LHV$, $\eta_p = TV/\dot{KE}$ and $\dot{KE}$ is the rate of kinetic energy added to the engine, LHV and $\dot{m}_f$ are the lower heating value and mass flow rate of fuel, T is the vehicle thrust, and V its velocity.

Table 10. Mission design and operational decision variables for the PS (inlet, nozzle, combustor) and AFS-A [7].

Variable		Classification	Symbol	Imposed Limits
Inlet	Forebody position [m]	Design decision	X_{fb}	$0.35L_{veh} \leq X_{fb} \leq 0.65L_{veh}$
	Cowl position [m]	Design decision	X_{cowl}	$0.45L_{veh} \leq X_{cowl} \leq 0.77L_{veh}$
	Ramp 1 position [m]	Design decision	X_{ramp1}	$0.02L_{veh} \leq X_{ramp1} \leq 0.33L_{veh}$
	Forebody angle [°]	Design decision	θ_{fb}	$1 \leq \theta_{fb} \leq 6$
Comb.	Combustor length [m]	Design decision	L_{comb}	$0.02L_{veh} \leq L_{comb} \leq 0.33L_{veh}$
Noz.	Nozzle expansion angle [°]	Design decision	θ_{nozz}	$8 \leq \theta_{nozz} \leq 18$
	Percent nozzle length	Design decision	$\%_{nozz}$	$0 \leq \%_{nozz} \leq 0.25$
AF	Angle of attack [°]	Design and Operational decisions	α_0	$0.1 \leq \alpha_0 \leq 6$

The algorithm used in the optimization is a heuristic algorithm, i.e. a genetic or evolutionary algorithm called QMOO, which stands for Queuing Multi-Objective Optimizer (QMOO), also known as Moo-LENI. It was designed by Leyland and Molyneaux at the Laboratoire d'Energétique Industrielle (Laboratory of Industrial Energy Systems ' LENI) at the Ecole Polytechnique Fédérale de Lausanne (EPFL) [38]. This software was developed specifically for the challenges encountered in optimizing complex energy systems. QMOO creates groups of solutions which evolve quasi-independently insuring that diversity is maintained, while also aggressively preserving only the best solutions. In addition, clustering is utilized to identify and surpass local optima. Consequently, QMOO has proven a valuable tool for energy systems optimization in many applications [38].

The optimization process for each problem begins with QMOO randomly selecting an initial set of values for the decision variables summarized in Table 10. Values for these variables are fed to the hypersonic vehicle program and upon successful completion, an objective function value is generated. For configurations in which the constraints of the vehicle program are not met, a severely penalized objective function is delivered to the optimizer in order to promote the choice of a better solution. The optimizer deals only with decision variable and objective function values. Every ten generations[12], the optimizer outputs a file containing the state of the current population, i.e. the objective function value and associated independent variable values.

[12] Note that a typical single generation in our case involved anywhere from 100 to 130 separate complete simulations of the vehicle flying its entire mission. A single optimization run required anywhere from fifty to a hundred and fifty thousand simulations spanning several days.

The optimization is manually stopped when the user identifies that convergence has occurred i.e. no further significant change in the objective function value has been observed for many generations. The coupling of the hypersonic vehicle model and QMOO is possible because both are implemented in MATLAB™. Six processors, with speeds ranging from 1.5 to 3.05 GHz, RAMs from of 512 to 1000 MB, and hard drives from 10 to 80 GB, were used independently throughout this study and each optimization was rerun several times to give confidence in the repeatability of the results.

2.6 RESULTS AND DISCUSSIONS

A selected set of results from both Markell [6] and Brewer [7] are presented and discussed here. For the complete set, the reader is encouraged to read these M.Sc. theses in detail. They can be downloaded from http://scholar.lib.vt.edu/theses/. In the first of these the results of a preliminary analysis using exergy methods for optimal combustor length prediction are presented. Next a number of individual hypersonic vehicle component investigations are conducted to gain insights into the hypersonic vehicle and its relation to exergy destruction. The results of these investigations are presented and discussed following the preliminary analysis. This is followed by the presentation of the PS optimization results which are given along with a fixed geometry PS analysis in order to investigate the trends of the PS operating at different flight Mach numbers. Finally, individual mission segment optimizations as well as partial mission (a three-segment mission) optimizations are presented and discussed, specifically looking at the use of exergy measures in the optimization of hypersonic vehicle configurations.

In the second thesis, several investigations are performed for the integrated hypersonic vehicle flying the six-segment mission described above. These include the impact of objective function choice on vehicle geometry and fuel mass fraction as well as a discussion of the optimization process and its results. In addition, the integrated hypersonic vehicle model itself is explored and compared to other models in the literature. Furthermore, the impact of mission segment discretization is addressed as is the performance of the integrated vehicle compared to vehicles optimized for a single mission segment. The usefulness of an exergy approach for overall vehicle synthesis/design is also examined.

In this report, we present and discuss some of the results obtained from the exergy analysis of the hypersonic vehicle by Markell [6]. This is then followed by results from Brewer [7] on the impact of mission segment discretization followed by a comparison between the optimum

mission-level integrated vehicles developed and those optimized based on a single mission segment. We begin, however, with a presentation of some of the results for model validation and exploration.

2.6.1 VALIDATION RESULTS AND VEHICLE COMPONENT/SUBSYSTEM CHARACTERISTICS

Though there is little information in the literature on hypersonic vehicle performance (there appears to be none for which a mission-level analysis is performed), this section compares the results of the vehicle model developed and implemented in the present research to others where possible and where not explores vehicle component and subsystem characteristics and performance. For example, to validate the performance characteristics of the combustor, the model was compared by Markell [6] against data supplied by Riggins [39]. Table 11 shows the data for both models at the inlet entrance (zero meters), combustor entrance (five meters), nozzle entrance (six meters), and engine exit (eleven meters). As can be seen, the differences between models are slight.

Table 11. Combustor model comparison/validation [7].

	Riggins Model [39]				Thesis Model [6,7]			
x (m)	M	T (K)	P (N/m^2)	u (m/s)	M	T (K)	P (N/m^2)	u (m/s)
0	12.0	200	1000	3400	12.0	200	1000	3400
5.0	6.22	679	70900	3260	6.26	674	70400	3260
6.0	1.72	4350	647000	2280	1.73	4340	646000	2290
11.0	5.12	1110	5500	3420	5.11	1120	5540	3420

Comparisons were also made for combustor length as a percentage of total length. The results of this comparison include combustor lengths for the theses model ranging from 2.1 to 4.4 percent of the vehicle length. Bowcutt's [36] optimal Mach 10 accelerator vehicle had a combustor length of 1.8 percent of the vehicle length, while Riggins [31] vehicle combustor length was estimated as 5 percent of the vehicle length. Starkey's two-dimensional model utilized combustor lengths of 7.1 to 8.2 percent of the vehicle length for Mach 8 and Mach 10 periodic trajectory cruises [40]. It should be noted that these comparisons should be viewed qualitatively, since each vehicle is designed for a different purpose, and each utilizes its own unique combustor model. As a brief note on the equivalence ratio, they were found to vary from 0.14 to 0.84 for the various vehicle designs in this comparative study. Though 0.14 seems quite

small, Bowcutt optimized a Mach 15 cruise vehicle with an equivalence ratio as low as 0.0675 [36].

A final validation for the PS model is done in order to determine the influence of step size

Table 12. Flow properties for a thrust efficiency-based objective function baseline vehicle over the entire hypersonic mission [7].

Mission Segment	Location	M	V [km/s]	P [kPa]	P_t [kPa]	T [K]	T_t [K]	$\dot{m}$ [kg/s]	γ	α [°]
Mach 6 - 8 Acceleration	Freestream	7	2.094	2.475	10.25	221.8	2395	141.9	1.4	1.9
	Inlet	8.093	2.091	2.929	30.83	165.5	2333			
	Combustor	2.924	1.724	215.8	7.070	861.3	2334			
	Nozzle	1.203	1.129	846.2	1964	2206	2645	143.6	1.275	
	Exit	4.752	2.384	2.718	1894	631.0	2591			
	Top Surface	6.940	2.092	2.616	10.25	225.3	2396	141.9[1]	1.4	
	Cowl	6.650	2.084	3.411	10.21	243.3	2395			
Mach 8 Cruise	Freestream	8	2.403	1.901	18.56	223.5	3084	124.1	1.4	1.6
	Inlet	8.261	2.394	2.714	32.65	208.1	3048			
	Combustor	2.888	1.963	219.8	6.819	1145	3055			
	Nozzle	1.478	1.443	626.8	2116	2396	3107	125.6	1.272	
	Exit	4.893	2.606	2.420	2118	712.9	3033			
	Top Surface	7.851	2.399	2.148	18.56	231.5	3085	124.1	1.4	
	Cowl	7.625	2.394	2.585	18.49	244.3	3085			
Mach 8 - 10 Acceleration	Freestream	9	2.712	1.502	31.70	225.1	3872	109.9	1.4	1.1
	Inlet	8.559	2.700	2.375	36.02	246.7	3861			
	Combustor	2.827	2.195	226.4	6.402	1494	3882			
	Nozzle	1.633	1.689	531.9	2256	2700	3663	111.2	1.268	
	Exit	5.019	2.853	2.174	2353	814.9	3562			
	Top Surface	8.670	2.706	1.917	31.64	241.4	3871	109.9	1.4	
	Cowl	8.676	2.706	1.907	31.61	241.1	3871			
Mach 10 Cruise	Freestream	10	3.023	1.204	51.10	226.5	4757	97.60	1.4	0.9
	Inlet	8.687	3.007	2.220	37.12	296.9	4778			
	Combustor	2.801	2.350	226.7	6.162	1872	4809			
	Nozzle	1.750	1.925	468.3	2380	3061	4297	98.74	1.264	
	Exit	5.122	3.112	2.007	2592	933.9	4164			
	Top Surface	9.529	3.016	1.654	50.93	248.3	4758	97.60	1.4	
	Cowl	9.676	3.018	1.496	50.99	241.1	4756			
Mach 10 Turn	Freestream	10	3.023	1.204	51.10	226.5	4757	97.54	1.4	2.1
	Inlet	7.911	2.966	3.025	27.47	348.3	4708			
	Combustor	2.946	2.476	210.1	7.116	1751	4790			
	Nozzle	1.811	1.967	450.3	2520	2981	4274	98.69	1.265	
	Exit	5.126	3.102	2.101	2715	925.6	4142			
	Top Surface	9.953	3.022	1.241	51.04	228.5	4756	97.54	1.4	
	Cowl	9.264	3.011	1.975	50.44	261.9	4757			
Mach 10 - 8 Deceleration	Freestream	9	2.712	1.502	31.70	225.1	3872	109.9	1.4	0.9
	Inlet	8.687	2.702	2.248	37.58	239.7	3857			
	Combustor	2.801	2.188	229.5	6.238	1512	3885			
	Nozzle	1.622	1.682	535.6	2235	2711	3666	111.2	1.268	
	Exit	5.020	2.855	2.156	2339	815.6	3564			
	Top Surface	8.613	2.705	2.000	31.61	244.5	3872	109.9	1.4	

on the accuracy of the differential marching scheme used to calculate the flow properties of the PS. The results show that using a step size based on 1000 steps causes a deviation of only 1% from the results found with a step size based on 10,000 steps. Since the latter step size complicates an already large computational burden which requires hundreds of thousands of mission-level integrated vehicle evaluations performed during the optimization process, the former step size base don 1000 steps is used throughout.

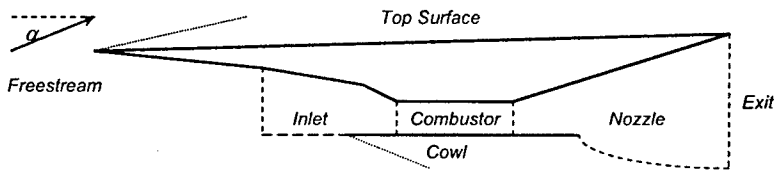

Figure 31. Hypersonic vehicle flow condition boundaries [7].

Now, to explore the temperatures, pressures, Mach numbers, and general flow conditions over the hypersonic regime studied here, some values of component *entrance/exit* conditions are determined for an initial (baseline) solution. Figure 31 shows the locations of the properties discussed while Table 12 above gives their values. Each value given in the table is the value at the entrance to each component. For the inlet, the value in the table is given after the forebody energy addition and forebody shock.

Much can be gained from examining and comparing the values given in table 12 over the various components and mission segments. For example, all of the top surface Mach numbers are less than the corresponding freestream Mach numbers for each mission segment, indicating that an oblique shock is occurring, or that the physical angle of the top surface is greater than the vehicle angle of attack. The constant specific heat ratio, γ, at the nozzle entrance and exit for each mission segment follows from the assumption that the nozzle flow is assumed to be frozen. The small change in flow properties from freestream to cowl is a result of the small oblique shock due to the angle of attack. Practically, if forebody and first and second inlet ramps are meant to converge before the cowl lip to avoid high temperatures, an expansion would occur right beneath the lip to follow the geometry of the cowl wall, yielding a similar flow Mach number as a consequence of an equal total flow turning angle (the angle of attack). However, property variations and total pressure losses would result from the irreversibilities associated with the forebody and inlet shocks, affecting frictional and pressure forces acting beneath the vehicle. The small static pressure change from freestream to inlet and the large static pressure

change from inlet to combustor over each of the segments illustrate the purpose behind including the forebody in the AFS-A and inlet in the PS. Of course, their contributions to aerodynamic forces and moments on the vehicle should be examined as well. These effects are discussed in Brewer [7].

The benefit of the shock-on-lip inlet design utilized for this research is also evident from Table 12. The angles of attack (α), none surpassing 2.1 degrees, illustrate the sensitivity of the vehicle as well as the capability of the inlet control system to maintaining relatively level flight throughout the mission segments. Furthermore, despite the large variation in freestream Mach number, the inlet Mach number varies through each mission segment between just Mach 7.91 and Mach 8.69. For a fixed geometry vehicle, this allows the greatest possibility of mass capture. The forebody angle and incoming Mach number (after flow manipulation via energy interaction) are both fixed entering the inlet. The reason for the variance in inlet Mach number is due to changing angle of attack. As a result, the need for a second energy interaction before the inlet ramp to maintain shock-on-lip becomes apparent. The trade-off of this design is that, though maximum flow is captured and the Mach number is constant, temperatures and pressures vary greatly at the inlet entrance (compare 165.5 °K for the Mach 6 to Mach 8 acceleration versus 348.3 °K for the Mach 10 turn). This model would not be feasible if the combustor entrance constraints could not be met. Fortunately, they can. Furthermore, an in-depth audit found in Brewer [7] of the shock-on-lip inlet design shows that its benefit in avoiding shock ingestion or mass spillage throughout the entire mission, is significant to overall vehicle performance. In fact, Markell shows that mass spillage can cause a reduction in thrust of 50 percent for a Mach 9 designed vehicle geometry flying at Mach 7 [6]. In addition, the overall contribution of the tailoring system to the overall exergy destruction remains relatively constant from initial to final optimal solutions.

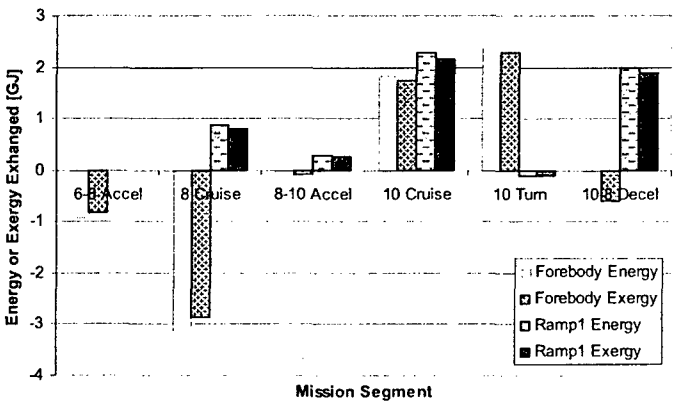

Figure 32. Required energy/exergy addition for the baseline thrust efficiency-based objective function vehicle [7].

With respect to this last point, Figure 32 shows the energy/exergy addition or removal required to

tailor the system to the desired shock-on-lip condition in each mission segment. Values above the horizontal axis correspond to energy/exergy being added, while those below indicate removal. Though its contribution to the overall exergy destroyed and lost is small, the magnitude of energy and somewhat less so of the exergy which must be introduced or removed is significant. However, the net exchange only represents a small fraction (on the order of 2 - 4%) of the total fuel exergy or exergy consumed. Nonetheless, since its magnitude is not negligible, designing and producing a flight-worthy physical mechanism capable of the dynamic energy/exergy exchange needed is indeed a difficult task. Even so, its potential benefits make it a challenge worth exploring.

Airframe and propulsive trim effects are also examined in detail in Brewer [7]. Only some of these are discussed here. For example, throughout the mission, the pitching moment for the PS produces a nose-down moment, while the AFS-A induces a nose-up moment. In every case, the primary contributor to the total untrimmed moment is the AFS-A. However, the magnitude ratio decreases significantly as the flight Mach number increases. This consistent nose-down trim requirement is not uncommon. NASA's X-43 utilizes an 800 lb slab of dense tungsten (which composes 29 percent of the vehicle's gross weight) placed in the forebody of the vehicle to shift the center of gravity forward [41]. Assuming this mass does not translate, an elevon would still likely be needed for trim during multiple mission segments. However, if the moment is partially trimmed by rearranging the center of gravity, such that the elevon need only traverse small positive and negative angles, then the drag on the vehicle can necessarily be reduced, since the elevon drag coefficient increases with deflection angle from a minimum value of C_{D0} at zero inclination to the flow. To measure the benefit of this approach, the savings in drag reduction must be compared to the effect of increasing the gross vehicle takeoff weight (if necessary). For these reasons, the exploration of an internally translating mass would likely be worthwhile. In this case, the drag reduction would have to be compared to the effect of increasing the vehicle volume, if necessary, to accommodate translation, in addition to the possibly increased initial weight.

As to the moments and forces of the baseline hypersonic vehicle of Table 12 which appear in Table 13 and Figure 33, a comparison to the literature leads to the following qualitative conclusions. For example, in all studies, the contribution and subsystem location of pitching moments shifts as flight Mach number varies, all of which is a drastic change from conventional

Table 13. Breakdown of moments due to surface forces for the baseline thrust efficiency-based objective function vehicle. For the vehicle shown in Figure 33, positive values indicate a clockwise (nose-up) moment [7].

	Moment Location	Mach 6-8 Accel.	Mach 8 Cruise	Mach 8-10 Accel.	Mach 10 Cruise	Mach 10 Turn	Mach 10-8 Decel.
Propulsive	Stream Thrust In, M_1	-224.1	-224.1	-223.6	-220.9	-220.7	-223.6
	Stream Thrust Out, M_7	209.1	198.3	237.3	213.2	190.6	210.4
	Inlet Ramp 1 Pressure, $M_{r1,p}$	124.8	120.5	113.1	108.9	125.7	110.2
	Inlet Ramp 2 Pressure, $M_{r2,p}$	-60.1	-58.0	-54.5	-52.4	-60.5	-53.1
	Cowl Lip Pressure, $M_{ci,p}$	205.2	198.0	185.9	179.0	206.6	181.2
	Nozzle Ramp, $M_{n,p}$	-310.1	-257.1	-273.5	-238.3	-249.1	-235.0
Airframe	Top Surface Friction, $M_{top,f}$	1.6	1.7	1.9	1.9	1.6	1.9
	Top Surface Pressure, $M_{top,p}$	-106.5	-87.5	-78.1	-67.4	-50.6	-81.5
	Forebody Friction, $M_{fb,f}$	-0.1	-0.1	-0.1	-0.1	-0.1	-0.1
	Forebody Pressure, $M_{fb,p}$	245.7	227.7	199.2	186.3	253.7	188.6
	Under Cowl Friction, $M_{c,f}$	-0.3	-0.3	-0.3	-0.3	-0.3	-0.3
	Under Cowl Pressure, $M_{c,p}$	-14.2	-10.8	-7.9	-6.2	-8.2	-7.6
Totals	Propulsive	-55.2	-22.4	-15.3	-10.5	-7.5	-9.9
	Airframe	126.2	130.8	114.7	114.3	196.1	101.0
	Untrimmed	71.0	108.4	99.4	103.8	188.6	91.2
	Elevon Trim, M_{elev}	-71.0	-108.6	-99.5	-104.0	-188.7	-91.2

aircraft. These shifts are more pronounced in the literature and include circumstances in which the PS can be much larger [36]. This is likely a result of different force accounting methods. For example, including the above forebody moments in the PS (as in a nose-to-tail force accounting method) could greatly change the AFS-A/PS pitching moment distribution. It is difficult, however, to make distinct comparisons to the literature since, for example, the distribution of moments given by Bowcutt not only include the nose-to-tail force accounting system, but also traverse a different range of Mach numbers with a different vehicle geometry, center of gravity, etc. [36]. All vehicles in the literature do consistently traverse small angles of attack (less than 8 or 10 degrees) [28,36]. The vehicles in

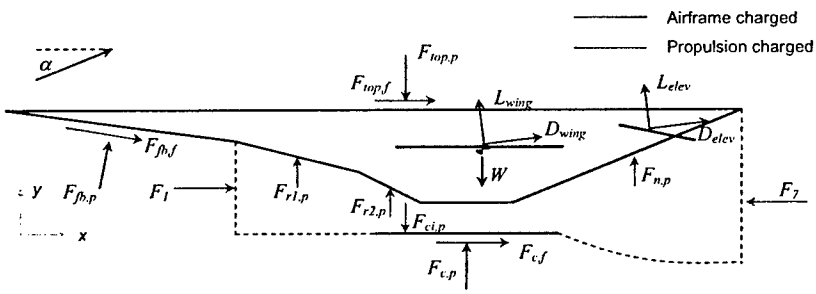

Figure 33. Airframe and propulsive forces acting on the hypersonic vehicle [7].

the present research do not exceed 2.5 degrees. This is a result of the inlet tailoring mechanism. Because the flow is manipulated prior to the forebody shock, larger angles of attack need not be traversed to adjust for the effect of flow spillage on vehicle thrust. Consequently, relatively few changes in pitching moment location and distribution occur for the optimum vehicles (compared to their respective baselines). This is not the case for the thrust and drag as is demonstrated in Brewer [7].

With respect to the latter, a plot of the drag contributions for each mission segment is given in Figure 34. As seen in the figure, the largest drag occurs during the initial mission segment. This is to be expected since the initial segment has the largest thrust minus drag requirement due to the inclination angle (to maintain constant dynamic pressure) and the fact that the fuel mass is the greatest (since none is assumed burned at the beginning of the segment). The weight component of drag is due to the inclination/ declination angles required during each respective climb/descend mission segment. As expected, this component reduces overall drag (or reduces the necessary thrust required) for the Mach 10 to Mach 8 deceleration, which requires a negative thrust minus drag value to decelerate. Also evident is that the wing and elevon components of drag for the Mach 10 turn account for 56 % of the drag, while in all other segments they total less than 30 %. This result is the combination of the increased load factor for the turn and that the largest trimming moment is required. As evidenced by the moments in Table 13, the largest wing area and elevon deflection angle are required during this segment. As will be shown, this is the case for all of the optimized vehicles. The larger drag contribution of the elevon (and hence larger lift, since both elevon and wing are diamond airfoils) implies that there exists opportunity for further geometric optimization between the wing and elevon. For

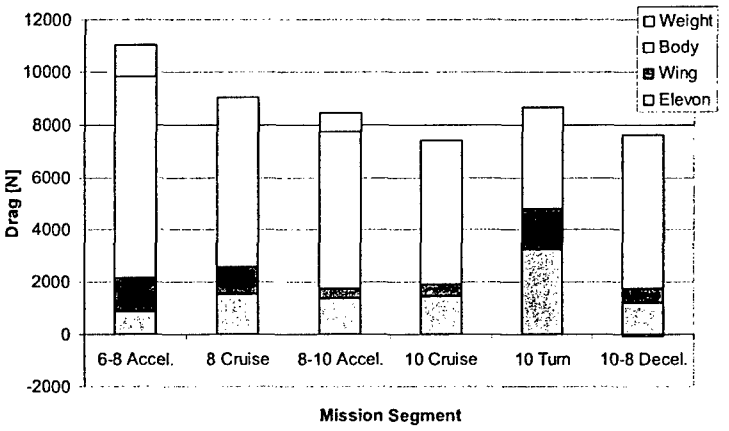

Figure 34. Component contributions to overall vehicle drag per mission segment for the baseline thrust efficiency-based objective function vehicle [7].

this research, the elevon area and location are fixed while the wing is attached to the vehicle at fixed angle of attack (zero) and acts through the vehicle center of gravity. Varying these parameters one might find only a wing *or* elevon is necessary. However, this would prove a multi-iterative solution procedure beyond the scope of the present research. The assumptions used here facilitate the speedy and accurate iteration and resolution of vehicle forces.

Finally, Table 14 shows the contributions of PS and AFS-A to overall vehicle lift for the baseline hypersonic vehicle geometry. The effective weight for each segment is the amount of lift the vehicle must provide based on the load factor. As given in Table 9, the load factor for all mission segments but the turn is one. For all segments other than the turn, the lift required is equal to the weight of the vehicle. For the turn, the lift required is double the weight (load factor equal to two). The total lift and effective weight are equal in all cases because unlike the iterative trim and throttling processes, the wing area is solved to precisely yield the lift needed (in the form of a wing area solved to several decimal places), so long as the required area is less than the maximum value (again constrained to be less than 9.6 m^2).

Table 14. PS and AFS-A contributions to overall vehicle lift for the baseline hypersonic vehicle [7].

	Mach 6-8 Accel.	**Mach 8 Cruise**	**Mach 8-10 Accel.**	**Mach 10 Cruise**	**Mach 10 Turn**	**Mach 10-8 Decel.**
Propulsive Lift [kN]	69.065	58.138	61.078	54.003	57.172	53.361
Airframe Lift [kN]	-8.240	1.155	-5.650	-0.738	40.589	-9.192
Total Lift [kN]	60.825	59.293	55.428	53.265	97.761	44.169
Effective Weight [kN]	60.825	59.293	55.428	53.265	97.761	44.169

2.6.2 EXERGY ANALYSIS RESULTS

An assortment of hypersonic vehicle component investigations were conducted to provide insights into the relationship between the design decision variables and the rate of exergy destruction and thrust as well as other performance measures. The rate of exergy destruction due to irreversibilities is directly proportional to the rate of entropy generation where the proportionality factor is simply the absolute temperature of the "dead state" (environment)[13] [15,19]. It is worth mentioning that the results presented in this section are a reflection of the

[13] Note that the "dead state", from a thermodynamic point of view, does not have to "float" for aerospace applications because the "dead state" is only a reference state which means that the value of "exergy" as any thermodynamic property can only be determined in relative terms, i.e. relative to a reference state.

methods chosen to model each component and, therefore, different hypersonic vehicle models may produce varying results. However, this does not undermine the fact that much knowledge can be gained from these exergetically based parametric studies.

Specific thrust[14] versus specific exergy[15] destruction as a function of the design decision variables is plotted in Figures 35 to 37. For these trade studies, the flight Mach number and the design Mach number are fixed at 9, i.e. no energy exchange with the freestream flow occurs. Table 15 displays the values of the design decision variables used in these studies as well as the respective ranges over which they were varied. The ranges of the forebody deflection angle and the first ramp length were limited to those specified in Table 15 in order to avoid violating the constraints imposed upon the inlet component, i.e. minimum/maximum inlet exit Mach number, minimum inlet exit pressure, etc. The forebody length and cowl position were not varied because: (a) it was difficult to find a range for which these variables, in combinations with each other and the other inlet design decision variables, satisfied all inlet constraints (with the remaining design decision variables fixed) and (b) no observable trends occurred when these variables were varied in conjunction with each other or another inlet design decision variable. Also, note that the $\%_{cowl}$ variable in this table is identical to the $\%_{nozz}$ given in Table 10.

Table 15. Fixed values and ranges for the design decision variable for component audits [6].

Design Variable	X_{fb}	X_{cowl}	X_{ramp1}	θ_{fb}	α	θ_{nozz}	L_{comb}	$\%_{cowl}$
Fixed Value	8.4	13.5	2.75	2.0	1.0	18.0	0.5	0.125
Range	—	—	2.7 – 3.5	1.75 – 6.25	—	8.0 – 18.0	0.5 – 1.5	0 – 0.25

Figure 35 displays the effect that the forebody angle and first ramp length have on the specific thrust and the specific exergy destruction of the PS. In this figure, the point of greatest temperature and pressure ratio and lowest inlet exit Mach number occurs at $\theta_{fb} = 6.5^{\circ}$ and $X_{ramp1} = 3.5$ and the point of smallest temperature and pressure ratio and largest inlet exit Mach number occurs at $\theta_{fb} = 1.75^{\circ}$ and $X_{ramp1} = 2.7$. It is apparent that at a fixed θ_{fb}, an increase in X_{ramp1} produces an increase in specific thrust and an appreciable increase in specific exergy destruction.

[14] Specific thrust is the thrust divided by the mass flow rate of air.
[15] Specific exergy destruction is the rate of exergy destruction divided by the mass flow rate of air.

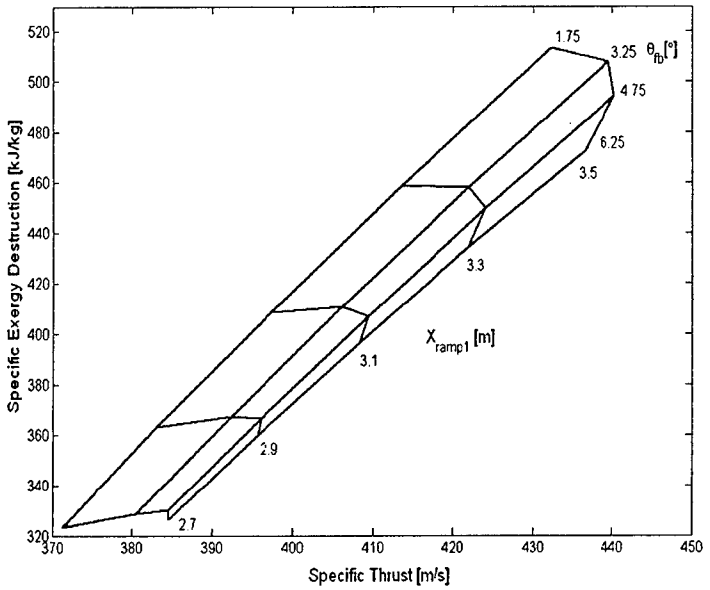

Figure 35. Specific exergy destruction versus specific thrust for a range of ramp lengths and forebody [6].

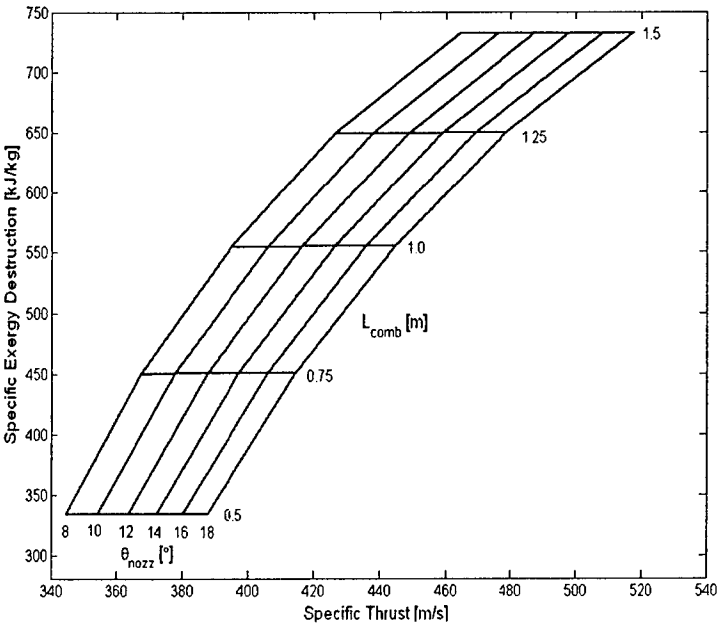

Figure 36. Specific exergy destruction versus the specific thrust for range of combustor lengths and nozzle expansion angles with the fixed design decision variable values listed in Table 15 [6].

Figure 35 also shows that at the longest X_{ramp1}, an increase in θ_{fb} results in a decrease in specific exergy destruction. However, as X_{ramp1} becomes smaller, the affect of a decrease in specific exergy destruction from an increase in θ_{fb} becomes less (even to the point where an increase in specific exergy destruction occurs). Finally, Figure 35 reveals: (a) two different geometries produce that same specific thrust; however, one destroys more specific exergy than the other and (b) the geometry producing the largest specific thrust does not produce the largest specific exergy destruction.

Figures 36 and 37 demonstrate the effects of combustor length, nozzle expansion angle, and percent cowl on the specific thrust and PS specific exergy destruction. As one would expect, an increase in L_{comb} causes a substantial increase in the specific exergy destruction. In addition, an increase in L_{comb} (for a given θ_{nozz}) produces an increase in specific thrust because a

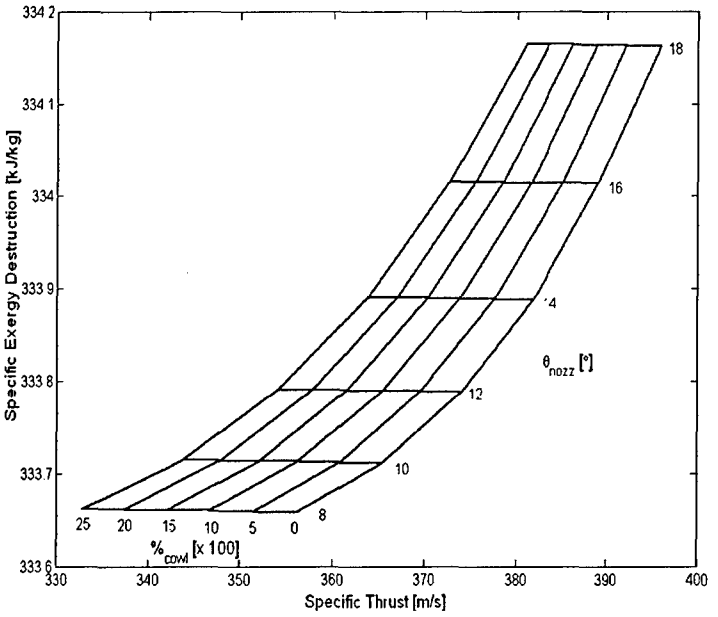

Figure 37. Specific exergy destruction versus the specific thrust for a range of nozzle expansion angles and percent cowl lengths with fixed design decision variable values listed in Table 15 [6].

longer combustor permits a more complete combustion which, in turn, allows for greater expansion through the nozzle (since the Mach number is closer to 1). Therefore, from the standpoint of Figure 36, it appears beneficial to have the shortest combustor and the largest θ_{nozz} to produce a given specific thrust. Also, from these figures, it is apparent that θ_{nozz} and $\%_{cowl}$ have minimal influence on the PS specific exergy destruction. A larger θ_{nozz} produces a larger specific thrust while a smaller $\%_{cowl}$ produces a larger specific thrust. Although it may seem best to operate the vehicle without any cowl extension into the nozzle, an extension may be needed to help reduce the large nozzle surface forces and moments inflicted upon the vehicle. This trend is shown in Figure 6-6 of Markell [7] where the larger cowl extensions act to counterbalance the surface forces and moments.

The inlet compression efficiency and inlet kinetic energy efficiency are plotted with the specific exergy destruction as a function of forebody angle and ramp length in Figures 38 and Figure 39. The kinetic energy efficiency is defined as the ratio of the square of the velocity that the compression system exit flow would achieve if it were isentropically expanded to the freestream static pressure to the square of the freestream velocity [17]. The kinetic energy efficiency is a direct measure of the preservation of kinetic energy, the most important quantity in scramjet propulsion for thrust production. The kinetic energy efficiency is near 1 at most large Mach numbers; therefore, at least three significant figures are needed to insure acceptable accuracy. Finally, the adiabatic compression efficiency is a function of the flight Mach number, kinetic energy efficiency, and the inlet static temperature ratio.

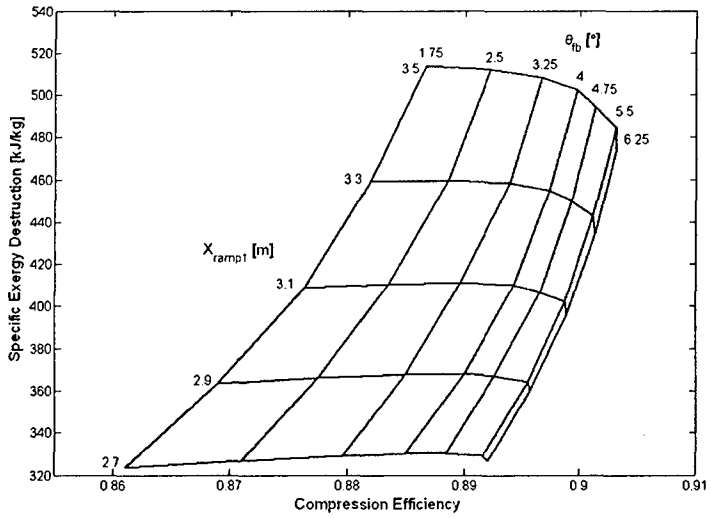

Figure 38. Specific exergy destruction versus the compression efficiency for a range of ramp lengths and forebody angles with the fixed design decision variable values listed in Table 15 [6].

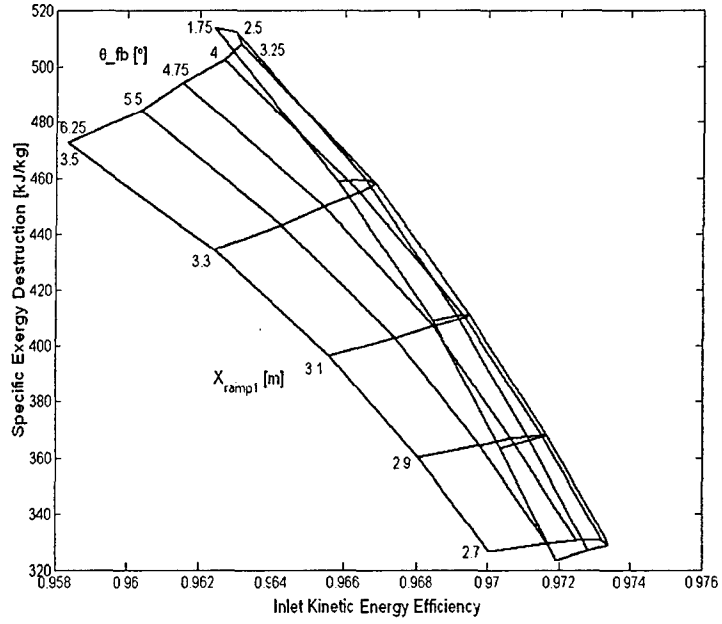

Figure 39. Specific exergy destruction versus the kinetic energy efficiency for a range of ramp lengths and forebody angles with the fixed design decision variable values listed in Table 15 [6].

From examining Figure 38, it appears that at a given θ_{fb}, it would be more reasonable to have a smaller X_{ramp1} because there is not much gain in compression efficiency with a longer X_{ramp1} while there is a rather large increase in specific exergy destruction. Of course, this all depends on the thrust demands of the hypersonic vehicle (refer to Figure 35).

Figure 39 reveals that a smaller X_{ramp1} for a given θ_{fb} is more desirable in terms of kinetic energy efficiency. Also, shown in Figure 6-8 is the fact that at $\theta_{fb} = 3.25^{\circ}$ the largest kinetic energy efficiency occurs for all ramp lengths. Although the scale depicted for the kinetic energy efficiency may seem inconsequential, small changes in the kinetic energy efficiency represent rather appreciable changes in inlet performance. A conclusion to be drawn from Figures 35 and 39 is that for certain required vehicle specific thrust the combination of the smallest X_{ramp1} and the largest θ_{fb} that can produce the required specific thrust

is most desirable to minimize the specific exergy destruction and maximize the compression efficiency.

Additional results from this parametric study can be found in Markell [6]. We now turn to the effects of single mission segment discretization on vehicle performance predictions found in Brewer [7].

2.6.3 EFFECTS OF SINGLE MISSION SEGMENT DISCRETIZATIONS

A requirement of a mission-level analysis is to utilize as many mission segments as needed to adequately, with varying degrees of fidelity, model the continuous mission which the aircraft must fly in going from point A to point B. In Brewer [7], for example, it is assumed that six segments are adequate for determining, for example, how the fuel burned affects total aircraft mass. One might reason that a six segment approximation, as opposed to a higher number approximation, necessarily requires a larger initial fuel mass since the mass fraction assumed at the beginning of each mission segment is fixed for the entire segment; and, hence, more mass is being carried along throughout each mission segment than is needed. However, in a highly integrated vehicle, it is difficult to know a priori how a change of mass may impact the vehicle performance. For example, a lighter mass might require a smaller wing area, reducing vehicle drag or if the wing area is already negligible, reduce the angle of attack of the vehicle, resulting in any number of possibilities regarding vehicle performance. Thus, a sensitivity study into the effect of further discretizations (i.e. more mission segments) on vehicle performance is performed.

Two cases, a Mach 8 to Mach 10 acceleration and a Mach 10 cruise are broken into one, two, and four segments to attempt to understand the effect of further discretization on the two types of mission segments considered in this research. For the Mach 8 to Mach 10 acceleration, the ninety second acceleration is broken into two 45 and four 22.5 sec segments. The effects on mission specific constraints are illustrated in Table 16[16]. It should be noted that the vehicle geometries flown in these segments are not optimized, i.e. a single working set of design decision variable values is used although the angle of attack selected happens to correspond to that which destroys the least exergy.

[16] A 5000 kg vehicle empty mass is assumed to carry only the fuel mass necessary for the segment in this discretization study. For example, the fuel mass fraction given by Table 9 for the Mach 8 to Mach 10 acceleration is $\pi_f = 0.0508$. This differs from the optimizations performed in Brewer [7] in which the empty mass of the vehicle is 4000 kg and the fuel mass fraction is the sum of the fuel mass fractions required for the segment of interest and the segments that follow.

Table 16. Effects of further discretizations on mission specific constraints for the Mach 8 to Mach 10 acceleration mission segment [7].

No.	Mission Segment	t_{ms} [s]	T_{veh}- D_{veh} [kN]	θ[°]	R [km]	Δh [km]	ΔV [m/s]	M_{avg} [m/s]
1	Mach 8-10 Acceleration	90	36.87	0.71	244.5	3.03	620	9
	TOTAL	90	-	-	244.5	3.03	620	-
1	Mach 8-9 Acceleration	45	36.60	0.78	116.0	1.58	309	8.5
2	Mach 9-10 Acceleration	45	36.80	0.64	129.8	1.45	311	9.5
	TOTAL	90	-	-	245.8	3.03	620	-
1	Mach 8-8.5 Acceleration	22.5	36.80	0.82	55.9	0.80	154	8.25
2	Mach 8.5-9 Acceleration	22.5	36.16	0.76	59.2	0.78	155	8.75
3	Mach 9-9.5 Acceleration	22.5	35.53	0.68	62.8	0.74	155	9.25
4	Mach 9.5-10 Acceleration	22.5	35.73	0.61	66.2	0.71	156	9.75
	TOTAL	90	-	-	244.1	3.03	620	-

As to the Mach 10 cruise, it is simply broken into two 300 and four 150 sec segments, requiring no modified constraint equations because constant altitude and speed is maintained (again, this is how cruise is defined in this research). The segments are limited to a maximum of four based on the time required to perform the evaluations, implying that having a program capable of accommodating real time updates or highly discretized evaluations would require either very simplified models or much greater computing power. A number of variables including fuel usage and exergy destruction plus fuel exergy loss for the different cases are shown in Table 17.

The Mach 8 to Mach 10 acceleration is somewhat affected by further discretizations though the effects are slight. A fuel savings of one to two percent results for each set of successive discretizations. This coincides with the slightly decreasing total exergy destruction plus fuel exergy loss values. Also noticeable is how the assumption of an average altitude affects the mass flow rates of air and equivalence ratios. As the density of air decreases, so does the mass flow rate. To maintain adequate thrust, the equivalence ratio increases accordingly. Though the totals change only slightly, the fuel usage and exergy destruction plus fuel exergy loss for each discretized part of the whole is noticeably greater the higher the average Mach number. The opposite trend is seen for the angle of attack, α. How these particular values of α are chosen (or for that matter the equivalence ratio, ϕ, the mass flow rate of air, $\dot{m}_{air}$, and the wing planform area, S_{wing}) is as follows. The vehicle flying the four-segmented mission segment is input into the optimization program until a set of values for α is found that can meet all four sub-segments.

The two-segmented and single mission segments are then simulated with the same set of values until the particular value or values that work(s) is (are) found.

Table 17. Effects of further discretizations on a number of variables including fuel usage and exergy destruction plus fuel exergy loss [7].

No.	Mission Segment	α [°]	ϕ	$\dot{m}_{air}$ [kg/s]	S_{wing}* [m^2]	Fuel Used [kg]	$Ex_{DES} + Ex_{FUEL\ LOSS}$ [GJ]
Mach 8-10 Acceleration							
1	Mach 8-10 Acceleration	0.8	0.74	107.7	4.736	210.5	14.39
	TOTAL	-	-	-	-	210.5	14.39
1	Mach 8-9 Acceleration	1.068	0.64	113.7	1.696	96.12	6.149
2	Mach 9-10 Acceleration	0.7	0.84	100.8	3.974	111.8	8.193
	TOTAL	-	-	-	-	207.8	14.34
1	Mach 8-8.5 Acceleration	1.068	0.58	117.3	4.354	44.93	2.786
2	Mach 8.5-9 Acceleration	1.0	0.68	110.1	0.9121	49.47	3.263
3	Mach 9-9.5 Acceleration	0.8	0.78	103.7	2.273	53.42	3.777
4	Mach 9.5-10 Acceleration	0.7	0.88	97.95	0.6090	56.94	4.315
	TOTAL	-	-	-	-	204.8	14.14
Mach 10 Cruise							
1	Mach 10 Cruise	1.030	0.28	104.5	0.3776	515.2	39.16
	TOTAL	-	-	-	-	515.2	39.16
1	Mach 10 Cruise	1.030	0.28	104.5	0.3776	257.6	19.58
2	Mach 10 Cruise	0.9	0.28	104.5	1.538	257.6	19.72
	TOTAL	-	-	-	-	515.2	39.30
1	Mach 10 Cruise	1.030	0.28	104.5	0.3778	128.8	9.790
2	Mach 10 Cruise	0.9	0.28	104.5	3.314	128.8	9.860
3	Mach 10 Cruise	0.9	0.28	104.5	1.538	128.8	9.922
4	Mach 10 Cruise	0.8	0.28	104.5	3.852	128.8	9.980
	TOTAL	-	-	-	-	515.2	39.55

*As indicated earlier, wing planform area is allowed to vary throughout the mission or in this case across a mission segment which is further discretized. This is necessary due to the highly constrained nature of the mission and to the difficulties of a fixed-wing geometry being able to meet all of the mission constraints.

Now, as to the Mach 10 cruise segment, very slight but consistent changes also occur. Contrary to the acceleration segment discretization, more exergy is destroyed and lost as the segment discretization progresses though these changes are much more subtle. Most of the values for the cruise segment remain unchanged for the discretization although variations in angle of attack and wing area do occur. Furthermore, for both the cruise and acceleration segments, having a variable wing area greatly facilitates level flight.

Finally, the initial assumption of a six segment mission operating at average velo-

cities and Mach numbers does not appear to hinder the results, as improved accuracy only totaled a few percent. However, discretization does provide insight into the parts of the segment which are the most and the least demanding.

2.6.4 INTEGRATED MISSION SYNTHESIS/DESIGN OPTIMIZATION RESULTS

In this section, results for the integrated mission-level synthesis/design optimization of a hypersonic vehicle based on the three different objectives discussed earlier (i.e. minimum fuel, minimum exergy destruction plus fuel exergy lost, and maximum thrust efficiency) are presented. To ensure some confidence in the globality of results, multiple optimizations were performed for each of the three objectives. This is, of course, not a proof of "globality" but simply an indicator that, due to the randomness of the evolutionary algorithm used and its ability to search the solution space of optimal solutions more thoroughly than more conventional gradient-based algorithms, finding a significantly better solution is not likely. Table 18 which presents the results for multiple optimizations of each objective furthermore shows that none of the objectives is exactly repeatable, though for the maximum thrust efficiency and minimum fuel objectives, two results very close to each other are found.

Table 18. Integrated hypersonic vehicle objective function values [7].

Run	Maximum Thrust Efficiency [%]	Minimum Fuel Mass [kg]	Minimum Exergy Destroyed Plus Fuel Exergy Lost [GJ]
1	34.52	1717	140.0
2	34.48	1720	142.3
3	32.97	1744	143.1

Table 19 shows the decision variable values for each of the best performing objective functions. Note that the optimal design decision value for the angle of attach, α_0, is that for the Mach 6 to Mach 8 acceleration mission segment. Simply looking at the numbers, it is difficult to draw any conclusions since the minimum fuel and minimum exergy objectives are both similar and different. To help clarify the differences, the vehicle geometries are plotted in Figure 40. As illustrated,

Table19. Optimum decision variable values for the best performing runs of each objective [7].

Objective	X_{fb} [m]	X_{cowl} [m]	X_{ramp1} [m]	θ_{fb} [°]	L_{comb} [m]	θ_{nozz} [°]	$\%_{nozz}$ [%]	α_0 [°]
Maximum First Law	8.909	13.75	3.258	1.790	0.568	17.43	0.0063	1.687
Minimum Fuel Mass	8.717	14.21	3.932	1.000	0.5000	16.67	0.5020	1.884
Minimum Exergy Destroyed Plus Fuel Exergy Lost	8.544	14.05	3.516	1.266	1.064	16.92	0.0100	2.129

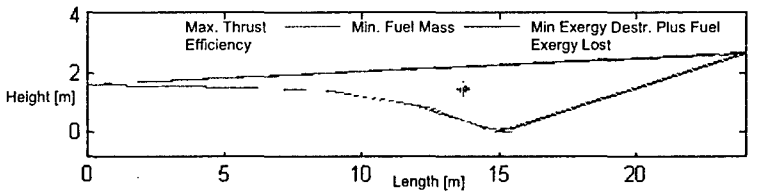

Figure 40. Optimum vehicle geometry for each of the three objectives [7].

the minimum exergy and minimum fuel objective vehicle shapes are nearly identical, while the maximized thrust efficiency results in a much broader vehicle. The plots show that the centers of mass are overlapping for the fuel mass and exergy cases, while the center of mass for the thrust efficiency objective is higher and more forward. The effect produced is a nozzle which begins sooner, resulting in a larger exit area, which enables the vehicle with this geometry to produce more thrust, as desired by the objective. Consequently, the frontal area is necessarily larger, which causes a larger ingestion of air, resulting in a stronger forebody shock and increased vehicle drag.

The only significant difference between the minimum exergy and minimum fuel cases is that the combustor for the former is double the length. This, as will be illustrated, allows less fuel exergy to be lost in the mixing layer of the combustor. The specific vehicle volumes are 23.59, 20.96, and 21.48 m^3 for the best performing maximum thrust efficiency, minimum fuel, and minimum exergy objectives, respectively. For a fixed mass, this essentially means that a less dense vehicle is produced by the maximum thrust efficiency objective. How each of these vehicles performs with respect to its optimum operational variable values over each of the mission segments is seen in Table 20.

Some trends are immediately noticeable. For example, the minimum fuel objective tends to fly at the highest angles of attack. Similarly, during the acceleration missions, the minimum fuel objective utilizes the largest equivalence ratios, followed by the minimum exergy and then maximum thrust efficiency cases. The body shape of the latter vehicle in general promotes a less aerodynamic form, as indicated by the wing areas. More times than not, this objective pushes the wing area near its maximum allowable area of 9.6 m^2, thus, incurring the associated drag penalty. Another interesting result is that all of the elevon deflection angles are positive and within the range of three to seven degrees. Therefore, a net unidirectional moment is always acting on the vehicle. The relatively small angles which are traversed by the vehicle elevon and angles of attack further demonstrate the sensitivity of the integrated vehicle to slight changes in flight conditions as well as the need for a precision control system.

Table 20. Mission segment optimum operational variable values [7].

Segment	α [°]	ϕ	S_{wing} [m^2]	$Q_{fb}^{\leftrightarrow}$ [GJ]	$Q_{rl}^{\leftrightarrow}$ [GJ]	ϖ_{elev} [°]	$\dot{m}_{cool}$ [kg/s]
Maximum Thrust Efficiency							
6-8 Accel.	1.687*	0.42**	9.556	-0.776	0	3.619	0.2822
8 Cruise	1.4	0.18	9.393	-2.601	0.416	4.399	0.4636
8-10 Accel.	0.9	0.76	5.662	-0.0851	0.193	4.769	0.6835
10 Cruise	0.7	0.26	5.952	1.364	1.774	4.749	0.917
10 Turn	1.9	0.28	9.410	2.157	-0.356	6.462	0.8731
10-8 Decel.	0.8	0.16	4.863	-0.574	1.288	4.129	0.6865
Minimum Fuel Mass							
6-8 Accel.	1.884	0.46	8.913	-0.7271	0	4.519	0.2649
8 Cruise	1.8	0.16	1.306	-2.326	1.159	5.230	0.4325
8-10 Accel.	1.1	0.82	1.504	-0.08985	0.1845	5.130	0.6441
10 Cruise	0.9	0.24	0.2408	1.187	2.711	4.989	0.8639
10 Turn	2.1	0.28	7.246	2.040	-3.466	6.640	0.8208
10-8 Decel.	1.0	0.14	0.4557	-0.6044	1.233	4.490	0.6471
Minimum Exergy Destroyed Plus Exergy Fuel Lost							
6-8 Accel.	2.129	0.40	0.1710	-0.7358	0	4.529	0.2815
8 Cruise	1.6	0.16	0.6670	-2.620	0.7300	4.439	0.4622
8-10 Accel.	0.8	0.76	1.028	0.1451	0.3104	4.149	0.6895
10 Cruise	0.6	0.26	4.207	0.8091	2.622	4.239	0.9265
10 Turn	2.2	0.28	2.114	1.955	-0.1140	6.519	0.8651
10-8 Decel.	0.7	0.14	3.717	-0.9298	1.979	3.750	0.6926

* The first angle of attack has more significant digits because it is decided by the algorithm. The other angles are found by inputting values within the range required in increments of 0.1 degrees.

** The thrust required by the constraining equations is found by throttling the equivalence ratio in increments of 0.02.

Table 21. Optimum vehicle characteristics for each mission segment [7].

Objective	**Max. thrust Efficiency**		**Min. Fuel Mass**		**Min. Exergy Destroyed Plus Fuel Exergy Loss**	
Segment	$\dot{m}_{air}$ [kg/s]	Thrust [kN]	$\dot{m}_{air}$ [kg/s]	Thrust [kN]	$\dot{m}_{air}$ [kg/s]	Thrust [kN]
6-8 Accel.	139.6	55.35	130.8	53.54	132.4	55.85
8 Cruise	122.1	13.13	114.4	9.015	115.8	9.850
8-10 Accel.	108.2	49.26	101.3	47.98	102.6	47.81
10 Cruise	96.01	9.789	89.97	7.430	91.06	8.040
10 Turn	95.97	10.13	89.92	8.975	91.00	8.346
10-8 Decel.	108.2	5.638	101.4	3.012	102.6	2.177

At first glance, the lower equivalence ratios during acceleration of the maximum thrust efficiency objective vehicle design seem to imply that less fuel is burned during those segments. However, careful attention must be paid to the resulting mass flow rates of air promoted by the geometries of each of the respective vehicles. Table 21 illustrates this relationship. The broad body of the maximum thrust efficiency objective requires a larger thrust via a larger mass flow rate in order to meet the constraining mission requirements given in Table 9, while the numbers for the minimum fuel and minimum exergy cases which are almost the same, are less.

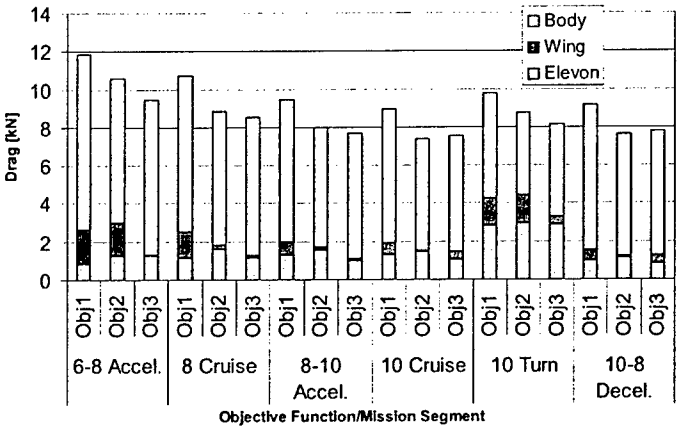

Figure 41. Drag contribution by airframe component for the optimum vehicles. Obj1, Obj2, and Obj3 are the maximized thrust efficiency, minimum fuel, and minimum exergy objective functions, respectively [7].

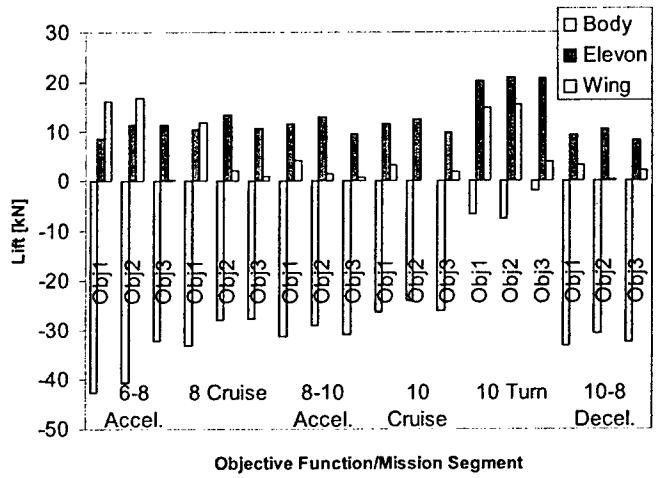

Figure 42. Lift contribution by AFS-A component for the optimum vehicles [7].

The total drag (broken down by AFS-A component) on the optimized vehicles over the mission is shown in Figure 41. As expected, the maximized thrust efficiency objective vehicle (objective 1 in the figure), which has a broader body, is subjected to the largest amount of drag throughout the mission. The minimum exergy objective vehicle (objective 3) has the least drag in all segments other than in the deceleration and Mach 10 cruise. In all cases, like the baseline vehicle discussed earlier, the body accounts for the majority of the drag. Also, as the wing areas given in Table 20 imply, the wing is a significant contributor to drag for every mission segment for the maximum thrust efficiency objective vehicle, while this is not the case for the minimum fuel and minimum exergy objective vehicles.

Figure 42 shows the lift provided by each AFS-A component. This figure shows that the mission segments which produce little wing drag for the minimum fuel and minimum exergy objective vehicles also add lift, as expected. For the Mach 10 turn, the elevon is the majority contributor to lift. In fact, it is a very significant contributor in every mission segment for all objectives, again illustrating the need to trim the nose-up pitching moment on the vehicles. This

is the case for all three objective functions because the vehicle is at its highest angle of attack during the Mach 10 turn (see Table 20), thus, minimizing the shock occurring on the top surface of the vehicle. The minimum exergy objective vehicle nearly has positive lift from the vehicle body as it is at the highest angle of attack of all vehicles and has a slender body like the minimum fuel objective vehicle.

For a detailed breakdown of the exergy destroyed or lost, Figure 43 shows where the exergy destruction and loss occur (i.e. in the inlet, combustor, etc.) during each mission segment. For all of the objectives, the combustor consistently proves to be the largest source of loss, except for the case of the Mach 8 to Mach 10 acceleration, in which case the fuel exergy loss is the greatest. For all three objectives, the inlet, nozzle, and AFS-A consistently destroy similar amounts of exergy.

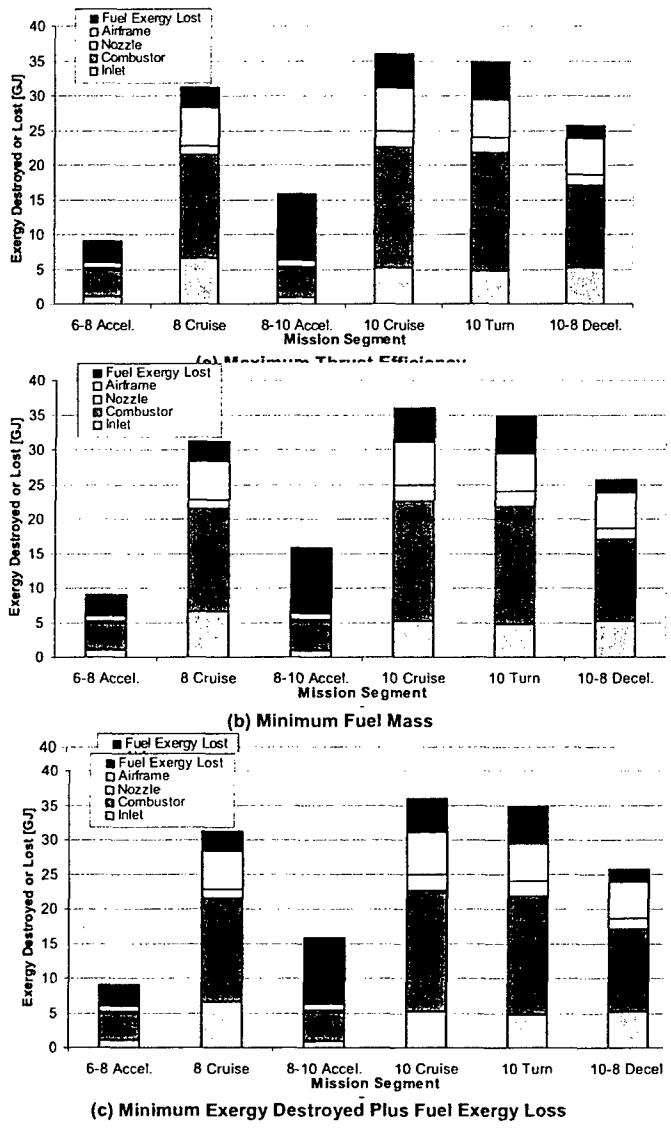

Figure 43. Exergy destroyed plus fuel exergy lost per mission segment for the best performing integrated vehicles [7].

Comparing objectives, the maximum thrust efficiency and minimum exergy objectives both have their largest exergy destruction and fuel loss occur during the Mach 10 cruise mission segment, while the most demanding segment for the minimum fuel objective is the Mach 10 turn. Perhaps the most interesting result is that while the minimum fuel and minimum

exergy objective vehicles both destroy and loose similar amounts of exergy, there is an obvious difference in where these occur. In each mission segment the exergy destroyed by the combustor is larger for the minimum exergy objective vehicle, while in a similar manner, the fuel exergy lost is much greater for the minimum fuel objective vehicle. In essence, there are two ways to arrive at the same efficiency of fuel use. A discussion of how the fuel mass is used for each of the objectives is discussed next.

Since each of the vehicles begin the mission with the same gross weight, the best vehicle burns the least fuel, and has more mass available for payload. This indicates that the fuel is being used most efficiently by meeting the constraints of the mission with the least exergy expended. The minimum fuel consumption should necessarily find the optimal vehicle configuration. How the more traditionally used maximum thrust efficiency objective and the more informative minimum exergy objectives compare to the minimum fuel mass objective is of interest here. The results are presented in Table 22 and Figure 44.

Table 22. Fuel mass used per mission segment [7].

Mission	Max. First Law [kg]	Min. Fuel Mass [kg]	Min. Exergy Destroyed + Fuel Exergy Lost [kg]
6-8 Accel.	155.0	159.0	139.9
8 Cruise	387.1	322.4	326.4
8-10 Accel.	217.2	219.6	206.0
10 Cruise	439.7	380.4	417.1
10 Turn	441.0	413.2	418.2
10-8 Decel.	270.8	222.0	224.8
Total	1910.8	1716.7	1732.4

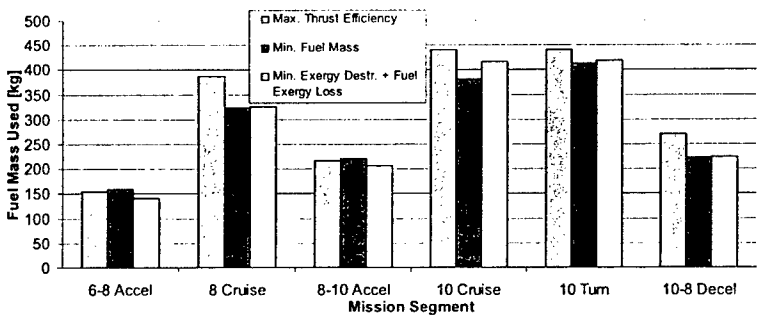

Figure 44. Fuel mass used per mission segment for each of the objective functions [7]

Note that there is not one optimal vehicle which uses the least fuel mass in all mission segments. Consistent with the conclusion that is drawn from the previous discussion on segment exergy destruction and fuel exergy loss, the maximum thrust efficiency objective vehicle consumes comparable quantities of fuel to those of the other two objective vehicles during the accelerations. Due to its poor performance in the other segments, however, the optimized thrust

efficiency objective vehicle results in one using 11.1 % more fuel than the minimum fuel case, from which one can conclude that *the maximum thrust efficiency objective is insufficient when performing an integrated vehicle synthesis/design.* The minimum exergy and minimum fuel cases, on the other hand, are much more alike. The best minimum exergy calculation yields a spent fuel mass of 1732, just 15 kg larger than the best performing minimum fuel case. This difference is less than one percent, leading to the conclusion that *the minimum exergy destruction plus fuel exergy loss and minimum fuel objectives are equivalent, at least in this case.* This last qualification is due to the fact that the character of the optimization algorithm used, i.e. a heuristic one, is such that at best it can only find a solution close to the global optimum. Thus, the conclusion of equivalency drawn here does not necessarily contradict the results found for the synthesis/design optimization of the AAF (advanced aircraft fighter) in *Section 1* above which shows, under similar circumstances, the minimum exergy objective to, in fact, be superior to the minimum fuel objective since the former produces a better optimum vehicle, i.e. one with less fuel usage. The discrepancy here is believed to be due to the difference in the nature of the optimization algorithms used: a heuristic versus a gradient-based one. The latter is able to home in on the global optimum provided, of course, that it has gotten close enough. Thus, in order to draw a firmer conclusion with regards to equivalency or not, future work on hypersonic vehicle synthesis/design optimization should apply a hybrid optimization approach which utilizes a heuristic to get close and a gradient-based algorithm to home in.

Table 23. Optimum actual mass fractions versus the predicted mass fractions for the integrated hypersonic vehicle.

Mission Segment	Fuel Mass Fraction, π_f			
	Assumed	Max. Thrust Efficiency	Min. Fuel Mass	Min. Exergy Destroyed + Fuel Exergy Lost
Mach 6-8 Acceleration	0.0521	0.0250	0.0256	0.0226
Mach 8 Cruise	0.0651	0.0624	0.0520	0.0526
Mach 8-10 Acceleration	0.0508	0.0350	0.0354	0.0332
Mach 10 Cruise	0.0812	0.0709	0.0613	0.0673
Mach 10 Turn	0.0759	0.0711	0.0666	0.0674
Mach 10-8 Deceleration	0.0300	0.0437	0.0358	0.0362
TOTALS	0.3551	0.3081	0.2768	0.2793

Now, as to the fuel mass fractions realized during the optimization of each of the objectives, they can be found in Table 23. The estimates given earlier in Table 9 are closest to the performance for the maximum thrust efficiency objective case, but all three cases prove to be over-predictions. In

this research, the empty mass is fixed at 4000 kg for an assumed fuel mass fraction of 0.3551. Thus, the gross takeoff weight of the vehicle is 6202 kg. The implication here is that, for a fixed initial vehicle mass, both the minimum fuel and minimum exergy objective cases allow for significantly more payload mass. However, if it is assumed that the payload is included in the empty mass of the vehicle, it also implies that the takeoff weight may be reduced through an iterative process since not all of the assumed fuel mass is needed.

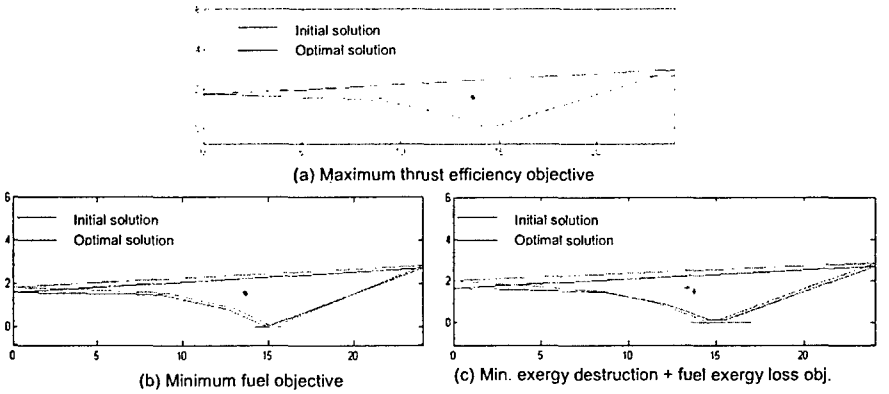

Figure 45. Vehicle geometry evolutions from the initial to the optimal solution for each objective function [7].

Finally, a view of the impact of each objective on the optimal vehicle geometry is provided in Figure 45, while Table 24 quantitatively shows some tendencies for the objectives. As seen in the figure, the optimal thrust efficiency objective drives the vehicle center of mass upward and toward the nose, increasing the vehicle volume, which is the opposite trend observed for the other two objectives. The nose of the maximum thrust efficiency objective vehicle remains constant, while the noses of the other two objective vehicles are driven downward (capturing less air), a result of the sleeker bodies needing less

Table 24. Mission characteristics for initial and optimal solutions [7].

		Max. Thrust Efficiency Obj.		**Min. Fuel Obj.**		**Min. Exergy Destroyed + Fuel Lost Obj.**	
		Initial	Optimal	Initial	Optimal	Initial	Optimal
Vehicle Volume [m^3]		21.03	23.59	22.59	20.96	25.26	21.48
Fuel Consumption [kg]		2528	1911	1902	1717	2197	1732
Exergy Destruction [GJ]		201.3	153.7	157.6	145.2	166.2	140.0
Thrust [kN]	6-8 Accel.	54.73	55.35	54.84	53.54	56.19	55.85
	8 Cruise	12.25	13.13	10.38	9.015	11.06	9.85
	8-10 Accel.	47.84	49.26	48.47	47.98	48.78	47.81
	10 Cruise	9.263	9.789	8.817	7.430	9.951	8.040
	10 Turn	9.942	10.13	10.46	8.975	10.72	8.346
	10-8 Decel.	4.813	5.638	3.934	3.012	4.010	2.177

thrust to meet the mission constraints. In all cases, the cowl extension into the nozzle is nearly eliminated, implying that perhaps it is not entirely necessary in the quasi one-dimensional models developed here. Furthermore, as seen in the table, fuel usage and exergy destroyed plus fuel exergy lost decreases significantly for all vehicles though it appears that only small changes in geometry occur. This is a further indication of the level of integration of the PS and AFS-A. The vehicle volume increases for the maximum thrust efficiency objective vehicle and decreases for the other two. The same trend occurs with thrust. As expected, the maximum thrust efficiency objective vehicle increases thrust while decreasing fuel usage. It does so while decreasing fuel usage by more than 20 percent. The minimum fuel and minimum exergy objective vehicles decrease fuel usage and thrust as they simultaneously decrease vehicle drag. *Since drag is neither directly nor indirectly taken into accounted in the maximum thrust efficiency objective function, it cannot produce the same fuel economy as the minimum fuel mass and minimum exergy objective vehicles for this mission-level analysis.*

2.6.5 SINGLE MISSION SEGMENT SYNTHESIS/DESIGN OPTIMIZATION RESULTS

Typically in aircraft synthesis/design (and for that matter, in the synthesis/design of most energy conversion systems), vehicles are synthesized/designed based on their most constraining mission segment or performance criterion. This section compares the results of such a synthesis/design methodology to the methodology utilized in this research work.

For this analysis, the single segment optimized vehicles found in Brewer [7] and summarized in Table 25 are each flown through the entire mission. Table 26 details the results.

Table 25. Optimum decision variable values for the best performing runs of each objective function [7].

Objective Function	X_{fb} [m]	X_{cowl} [m]	X_{ramp1} [m]	θ_{fb} [°]	L_{comb} [m]	θ_{nozz} [°]	$\%_{nozz}$	α_0 [°]
Max. Thrust Eff.	8.909	13.75	3.258	1.790	0.586	17.43	0.0063	1.687
Min. Fuel Mass	8.717	14.21	3.932	1.000	0.5000	16.67	0.5020	1.884
Min. Exergy	8.544	14.05	3.516	1.266	1.064	16.92	0.0100	2.129
Single Mission Segment Optimizations								
Mach 6-8 Accel.	8.443	14.62	3.702	1.006	1.030	15.70	12.74	1.506
Mach 8 Cruise	8.690	13.24	2.900	1.009	0.5286	10.46	19.25	1.081
Mach 8-10 Accel.	9.082	14.40	3.363	2.630	1.045	17.17	19.82	0.1000
Mach 10 Cruise	8.407	13.29	3.443	1.079	0.5537	12.93	12.50	0.4306
Mach 10 Turn	8.824	14.55	3.713	1.000	1.032	17.83	9.270	2.241
Mach 10-8 Decel.	8.537	12.98	3.030	1.000	0.5025	14.36	9.820	1.358

Only the Mach 6 to Mach 8 acceleration optimized single segment vehicle is capable of completing the entire mission. All other single segment optimized vehicles fail in this segment, while the vehicle for which it is specifically optimized completes the entire mission with "good" results (i.e. showing an improvement over each of the baseline configurations found for the objectives of the mission-level optimizations), implying that the Mach 6 to Mach 8 acceleration is indeed the constraining mission segment.

Table 26. Failure location of single segment optimized vehicles flown through the entire mission [7].

Mission Segment	Angle of Attack [°]	Failure Segment	Component/ Sub-System	Reason
Mach 6-8 Accel.	Completed Mission – see Figure 46			
Mach 8 Cruise	$\alpha \leq 2.0$	Mach 6-8 Accel.	Combustor	$M < 1$
	$\alpha > 2.0$	Mach 6-8 Accel.	Inlet	Shock-on-lip
Mach 8-10 Accel.	$\alpha \leq 1.7$	Mach 6-8 Accel.	Combustor	$M < 1$
	$\alpha > 1.7$	Mach 6-8 Accel.	Inlet	Shock-on-lip
Mach 10 Cruise	$\alpha \leq 1.9$	Mach 6-8 Accel.	Combustor	$M < 1$
	$\alpha > 1.9$	Mach 6-8 Accel.	Inlet	Conceptual diffuser $M < 2.2$
Mach 10 Turn	$\alpha \leq 2.0$	Mach 6-8 Accel.	Combustor	$M < 1$
	$\alpha > 2.0$	Mach 6-8 Accel.	Inlet	Conceptual diffuser $M < 2.2$
Mach 10-8 Decel.	$\alpha \leq 1.8$	Mach 6-8 Accel.	Airframe	$S_{wing} > S_{wing,\ max}$
	$\alpha > 1.8$	Mach 6-8 Accel.	Inlet	Shock-on-lip

Four failure types are noted for the unsuccessful single segment optimizations. The most common are that the Mach number in the combustor becomes subsonic before reaching the nozzle and that the energy exchange mechanism cannot maintain a shock-on-lip condition above certain angles of attack. At high angles of attack at Mach 10, the friction applied by the conceptual diffuser drives the Mach number below the required minimum value of 2.2 for the combustor entrance. Finally, the Mach 10 to Mach 8 deceleration vehicle makes it through the inlet, combustor, and nozzle, yet fails in the AFS-a because a larger than allowable wing area (lift) is required to balance the vehicle weight. Ultimately, a more comprehensive study in which various gross weights are examined would be of value.

Finally, the Mach 6 to Mach 8 acceleration single segment optimized vehicle performs the complete mission burning 1877kg of fuel with an exergy destruction and fuel exergy loss of

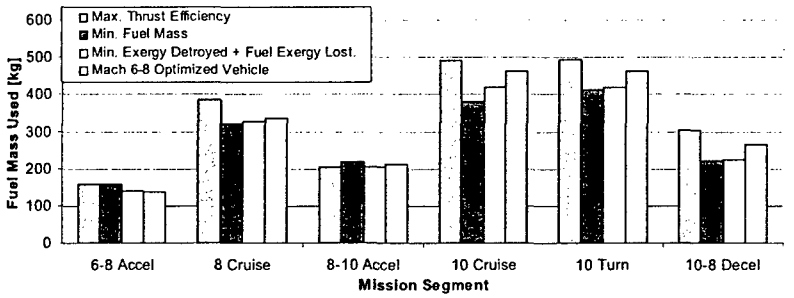

(a) Fuel Consumption per Mission Segment

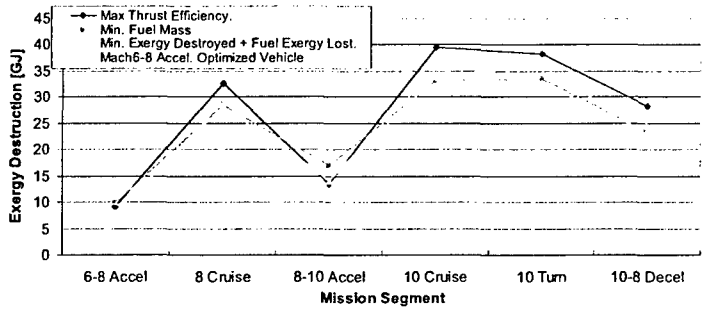

(b) Exergy Destroyed Plus Fuel Exergy Lost per Mission Segment

Figure 46. Performance characteristics for the Mach 6 to Mach 8 single segment optimized vehicle over the complete hypersonic mission envelope compared to the mission-level integrated vehicle optimizations [7].

145.8 GJ. This outperforms the maximum thrust efficiency objective mission-level optimized vehicle, but falls short of the minimum exergy and minimum fuel mission-level optimized vehicles. Figure 46 suggests that the small gains made during the Mach 6 to Mach 8 acceleration (versus the mission-level exergy and fuel objective vehicles) reduces its ability to perform well in other segments. This is, once again, an indication of the benefit of an integrated mission-level vehicle synthesis/design.

3. CONCLUSIONS

A lot of very useful research over the last decade has been focused on how to apply exergy analysis to aircraft system synthesis/design and operation (e.g., [6-14,21-25,31]). Since at least the 1960s, it has been demonstrated again and again for stationary systems that an exergy-based analysis has a significant advantage over that of an energy-based approach as a tool for energy systems synthesis/design. However, applying these same techniques, developed for and applied to stationary systems, to aerospace systems has required additional thought and work. As demonstrated above both for the advanced aircraft fighter system of *Section 1* and for the hypersonic aircraft system of *Section 2*, quantifying all the vehicle losses in terms of the rate of exergy destruction provides a common metric for the vehicle designer to identify where the

largest improvements in vehicle performance can be made which ultimately, of course, results in a lower amount of fuel consumption.

Even in optimization approaches, it has long been known that the use of an exergy-based approach can provide detailed information about why the synthesis/design is driven towards the optimum or even provide the basis for the optimization algorithm used to find the optimal synthesis/design. What has not been so obvious is its role as objective function. Nonetheless, it has been demonstrated any number of times in the literature that as long as the constraint space is the same, an energy-based objective produces the same optimum as that of the exergy-based objective provided that they are equivalent forms of the same thing, e.g., fuel consumption. This has been demonstrated once more in *Section 1* for the optimizations with objectives 1, 2, 4, and 5 of the advanced aircraft fighter system.

However, with the *active* (i.e. with losses and degrees of freedom) inclusion of the AFS-A, which is by definition not an energy system in the traditional sense, this equivalency between energy and exergy objectives properly interpreted no longer appears to hold, i.e. is not true at least for the case demonstrated in *Section 1* in the set of optimizations involving objectives 1 and 3. It is in fact the lack of a common currency, which is the case when an exergy-based approach is *not* used, that results in an inability to relate very different types of inefficiencies in one part of a system (such as those in the AFS-A) to those occurring in another part (such as those in the PS and ECS) which points generally to the need for *exergy* as the basis for both analysis and optimization even though for some systems and some problems energy may be sufficient at least at an objective function level. This conclusion is not necessarily contradicted by the conclusion of equivalency drawn in *Section 2* between the minimum exergy destruction plus fuel exergy loss and minimum fuel objectives. The discrepancy here is believed to be due to the difference in the nature of the optimization algorithms used: a heuristic versus a gradient-based approach. The latter used to generate the results of *Section 1* is able to home in on the global optimum provided, of course, that it has gotten close enough. The former used in *Section 2* to generate its results is one that at best can only find a solution close to the global optimum. Thus, in order to draw a firmer conclusion with regards to equivalency or not, future work on this same hypersonic vehicle synthesis/design optimization problem needs to be done with a hybrid optimization approach which utilizes a heuristic to get close and a gradient-based algorithm to home in.

As to the need for integrated mission-level synthesis/design in the types of complex systems considered in both *Sections 1 and 2*, the comparisons made in *Section 2* between the syntheses/designs found for single-segment optimized vehicles and those found using an integrated mission-level approach illustrate the necessity of the latter for arriving at an optimal vehicle synthesis/design. Though optimizing the most constrained mission segment yields a vehicle capable of completing the mission with good results, the best vehicle performance is found only through an integrated synthesis/design over the entire mission. Furthermore, the robustness of such an integrated approach is demonstrated in Brewer [7] by flying the optimized aircraft over an extended mission for which the flight ceiling, gross takeoff weight, and thrust requirements are increased. The result is that a capable vehicle is found after decision variable constraints are modified. The need for constraint modification is undesirable for any optimization process (as feasible decision variable value ranges may not be initially known) but necessary in an integrated hypersonic vehicle study due to the highly coupled nature of the PS and AFS-A.

Finally, it is also suggested that the use of exergy-based methods and integrated mission-level optimization approaches may show even more benefits for revolutionary concepts with even more inter-dependent subsystems. These include, for example, hypersonic vehicles with a number of additional highly integrated subsystems flown over complete missions which include takeoff and landing, reconnaissance aircraft with high power sensors, vehicle concepts with other high-energy payloads such as direct energy weapons, etc.

4. REFERENCES

1. Rancruel, D. F., von Spakovsky, M. R., 2004, "Use of a Unique Decomposition Strategy for the Optimal Synthesis/ Design and Operation of an Advanced Fighter Aircraft System," 10th *AIAA/ISSMO Multi-disciplinary Analysis and Optimization Conf.*, Aug. 30 - Sept. 1, Albany, N. Y.
2. Rancruel, D. F., von Spakovsky, M. R., 2003, "Decomposition with Thermoeconomic Isolation Applied to the Optimal Synthesis/Design of an Advanced Fighter Aircraft System," *International Journal of Thermodynamics*, ICAT, Istanbul, Turkey, September, vol. 6, no. 3.

3. Muñoz, J.R., von Spakovsky, M.R., 2003, "Decomposition in Energy System Synthesis / Design Optimization for Stationary and Aerospace Applications," *AIAA Journal of Aircraft*, special issue, Vol. 39, No. 6, Jan-Feb.
4. Rancruel, D. F., von Spakovsky, M. R., 2003, "A Decomposition Strategy Applied to the Optimal Synthesis/Design and Operation of an Advanced Fighter Aircraft System: A Comparison with and without Airframe Degrees of Freedom," *ASME–IMECE'2003*, ASME Paper No. 44402, N.Y., Nov.
5. Rancruel, D. F., 2002, "A Decomposition Strategy Based on Thermoeconomic Isolation Applied to the Optimal Synthesis/Design and Operation of an Advanced Fighter Aircraft System," M.S. thesis, Advisor: M. R. von Spakovsky, Mechanical Engineering Dept., Virginia Polytechnic Institute and State Univ., Blacksburg, VA.
6. Markell, K. C., 2005, "Exergy Methods for the Generic Analysis and Optimization of Hypersonic Vehicle Concepts," M.S. thesis, Advisor: M. R. von Spakovsky, Mechanical Engineering Dept., Virginia Polytechnic Institute and State Univ., Blacksburg, VA, February 2005.
7. Brewer, K. M., 2005, "Exergy Methods for Mission-Level Analysis and Optimization of Generic Hypersonic Vehicle Concepts," M.S. thesis, Advisor: M. R. von Spakovsky, Mechanical Engineering Dept., Virginia Polytechnic Institute and State Univ., Blacksburg, VA, April 2006.
8. Butt, J., 2005, "A Study of Morphing Wing Effectiveness in Fighter Aircraft Using Exergy Analysis and Global Optimization Techniques," M.S. thesis, Advisor: M. R. von Spakovsky, Mech. Eng. Dept., Virginia Polytechnic Institute and State Univ., Blacksburg, VA, Dec. 2005.
9. Periannan, V., 2005, "Investigation of the Effects of Different Objective Functions/Figures of Merit on the Analysis and Optimization of High Performance Aircraft System Synthesis/Design," M.S. thesis, Advisor: M. R. von Spakovsky, Mech. Eng. Dept., Virginia Polytechnic Institute and State Univ., Blacksburg, VA, Aug. 2005.
10. Roth, B., 2001, "A Work Potential Perspective of Engine Component Performance," AIAA Paper 2001-3300, July.

11. Riggins, D. 2003, "The Thermodynamic Continuum of Jet Engine Performance: The Principle of Lost Work due to Irreversibility in Aerospace Systems," *International Journal of Thermodynamics*, ICAT, Istanbul Turkey, vol. 6, no. 3.
12. Moorhouse, D. J., 2003, "Proposed System-Level Multidisciplinary Analysis Technique Based on Exergy Methods," *AIAA Journal of Aircraft*, Vol. 40.
13. Figliola, R.S. and Tipton, R., 2000, "An Exergy-Based Methodology for Decision-Based Design of Integrated Aircraft Thermal Systems," Paper No. 00WAC-92, SAE.
14. Paulus, D.M. and Gagglioli, R.A., 2000, "Rational Objective Functions for Vehicles," AIAA-2000-4852, Sept.
15. Gyftopoulos, E. P. and Beretta, G. P., 2005, *Thermodynamics – Foundations and Applications*, Dover Publications, New York.
16. gPROMS, 2004, Process Systems Enterprise Ltd., London, United Kingdom.
17. Heiser, W. H., and Pratt, D. T., *Hypersonic Airbreathing Propulsion.* AIAA, Inc., Washington, D.C., 1994.
18. Anderson Jr., J. D., *Hypersonic and High Temperature Gas Dynamics.* AIAA, Inc., Reston, VA, 1989.
19. Moran, M.J., "Availability Analysis: A Guide to Efficient Energy Use," ASME Press, New York, 1989.
20. Greene, G. C., "An Entropy Method for Induced Drag Minimization," SAE TP Series 892344, Sept. 1989.
21. Periannan, V., von Spakovsky, M.R., and Moorhouse, D. J., 2006, *Investigation of the Effects of Various Energy and Exergy-Based Figures of Merit on the Optimal Design of a High Performance Aircraft System, International Mechanical Engineering Congress and Exposition – IMECE'2006*, ASME Paper No. IMECE2006-14186, N.Y., N.Y., November.
22. Moorhouse, D. J., Hoke, C. M., and Prendergast, J. P., 2002, "Thermal Analysis of Hypersonic Inlet Flow with Exergy-Based Design Methods," *International Journal of Applied Thermodynamics*, Vol. 5, No. 4, Dec.
23. Riggins, D. W., McClinton, C. R., and Vitt, P. H., 1997, "Thrust Losses in Hypersonic Engines Part 1: Methodology," *Journal of Propulsion and Power*, Vol. 13, No. 2, Mar. - Apr.
24. Riggins, D. W., 1997, "Thrust Losses in Hypersonic Engines Part 2: Applications,' *Journal of Propulsion and Power*, Vol. 13, No. 2, Mar. - Apr.

25. Figliola, R. S, Tipton, R., and Li, H., "Exergy Approach to Decision-Based Design of Integrated Aircraft Thermal Systems," *Journal of Aircraft*, Vol. 40, No. 1, Jan.-Feb. 2003.
26. Schindel, L., 1999, "Effect of Non-uniform Nozzle Flow on Scramjet Performance," *Journal of Propulsion and Power*, Vol. 15, No. 2, Mar. – Apr.
27. Stalker, R. J. and Morgan, R. G., 1984, "Supersonic Hydrogen Combustion with a Short Thrust Nozzle," *Combustion and Flame,"* Vol. 57.
28. Curran, E. T., and Murthy, S. N. B., 2000, *Scramjet Propulsion - Progress in Astronautics and Aeronautics*, Vol. 189. AIAA, Inc., Reston, VA.
29. Riggins, D. W., Private Communication, July 2003 - July 2004.
30. Shapiro, A. H., *The Dynamics and Thermodynamics of Compressible Fluid Flow*, 1st Edition, John Wiley and Sons, New York, 1953.
31. Riggins, D. W., 1997, "Evaluation of Performance Loss Methods for High-Speed Engine and Engine Components", *Journal of Propulsion and Power*, Vol. 13, No. 2, March-April.
32. John, J. E. A., 1984, *Gas Dynamics*, 2nd Edition, Prentice Hall, Upper Saddle River, NJ.
33. Lehrach, R.P.C., 1987, "Thrust/Drag Accounting for Aerospace Plane Vehicles," AIAA Paper No. 1987-1966.
34. Numbers, K. , 1991, "Hypersonic Propulsion System Force Accounting," AIAA Paper No. 1991-0228.
35. Anderson Jr., J. D. , 2001, *Fundamentals of Aerodynamics*, 3rd Edition, McGraw-Hill, New York.
36. Bowcutt, K. , 1992, "Hypersonic Aircraft Optimization Including Aerodynamic, Propulsion, and Trim Effects," AIAA Paper No. 1992-5055.
37. Moorhouse, D. J., Private Communication, June 2003-August 2004.
38. Leyland, G. B. , 2002, *Multi-Objective Optimisation Applied to Industrial Energy Problems*, Department of Mechanical Engineering, University of Auckland, Ph.D. Dissertation.
39. Riggins, D. W. , 1996, "High-Speed Engine/Component Performance Assessment Using Exergy and Thrust-Based Methods," NASA Contractor Report 198271.
40. Starkey, R. P. , 2004, "Scramjet Optimization for Maximum Off-Design Performance," AIAA Paper No. 2004-3343.
41. Dornheim, M. , 2005, "A Breath of Fast Air," *Aviation Week and Space Technology*, April 5th.